

Star Formation in Nuclear Rings with the TIGRESS Framework

SANGHYUK MOON,^{1,2} WOONG-TAE KIM,^{1,2} CHANG-GOO KIM,³ AND EVE C. OSTRIKER³

¹*Department of Physics & Astronomy, Seoul National University, 1 Gwanak-ro, Gwanak-gu, Seoul 08826, Republic of Korea*

²*SNU Astronomy Research Center, Seoul National University, 1 Gwanak-ro, Gwanak-gu, Seoul 08826, Republic of Korea*

³*Department of Astrophysical Sciences, Princeton University, Princeton, NJ 08544, USA*

(Received; Revised; Accepted)

ABSTRACT

Nuclear rings are sites of intense star formation at the centers of barred galaxies. To understand what determines the structure and star formation rate (SFR; \dot{M}_{SF}) of nuclear rings, we run semi-global, hydrodynamic simulations of nuclear rings subject to constant mass inflow rates \dot{M}_{in} . We adopt the TIGRESS framework of Kim & Ostriker to handle radiative heating and cooling, star formation, and related supernova (SN) feedback. We find that the SN feedback is never strong enough to destroy the ring or quench star formation everywhere in the ring. Under the constant \dot{M}_{in} , the ring star formation is very steady and persistent, with the SFR exhibiting only mild temporal fluctuations. The ring SFR is tightly correlated with the inflow rate as $\dot{M}_{\text{SF}} \approx 0.8\dot{M}_{\text{in}}$, for a range of $\dot{M}_{\text{in}} = 0.125 - 8 M_{\odot} \text{ yr}^{-1}$. Within the ring, vertical dynamical equilibrium is maintained, with the midplane pressure (powered by SN feedback) balancing the weight of the overlying gas. The SFR surface density is correlated nearly linearly with the midplane pressure, as predicted by the pressure-regulated, feedback-modulated star formation theory. Based on our results, we argue that the ring SFR is causally controlled by \dot{M}_{in} , while the ring gas mass adapts to the SFR to maintain the vertical dynamical equilibrium under the gravitational field arising from both gas and stars.

1. INTRODUCTION

Nuclear rings were first identified in photographic plates as multiple “hot spots” near galaxy centers (Morgan 1958; Sérsic & Pastoriza 1965), which have turned out to be manifestation of compact yet vigorous star-forming regions (see also Kennicutt 1994; Kormendy & Kennicutt 2004, and references therein). They are thought to form as a result of gas redistribution due to a bar potential (e.g., Combes & Gerin 1985; Buta 1986; Shlosman et al. 1990; Garcia-Barreto et al. 1991; Buta & Combes 1996). Indeed, numerical simulations have consistently shown that the non-axisymmetric torque exerted by a stellar bar in disk galaxies causes gas to move radially inward along dust lanes and form a ring near the centers (e.g., Athanassoula 1992; Piner et al. 1995; Englmaier & Gerhard 1997; Patsis & Athanassoula 2000; Kim et al. 2012b; Kim & Stone 2012; Li et al. 2015). It is uncertain what determines the ring locations, but theoretical proposals suggest it may be determined by radial extent of periodic orbits caused by a bar potential (Bin-

ney et al. 1991; Regan & Teuben 2003), balance between centrifugal force and external gravity (Kim et al. 2012a), or shear reversal (Sormani et al. 2018). While bars are by far the most efficient agent driving mass inflow in galactic disks, other non-axisymmetric features such as spiral arms, elongated bulges, and ovals can also drive mass inflow to fuel starburst activity (e.g., Athanassoula 1994; Combes 2001; Kim & Kim 2014; Seo & Kim 2014; Kim et al. 2018a).

Observations indicate that the star formation rate (SFR) in the rings of normal barred galaxies spans a wide range $\sim 0.1 - 10 M_{\odot} \text{ yr}^{-1}$ (Mazzuca et al. 2008; Ma et al. 2018), while the total gas mass range in the rings is more limited, $\sim (1 - 6) \times 10^8 M_{\odot}$ (Sheth et al. 2005). The central molecular zone (CMZ), which is believed to be a nuclear ring in the Milky Way, contains gas mass of $\sim (3 - 7) \times 10^7 M_{\odot}$ (Pierce-Price et al. 2000; Molinari et al. 2011; Tokuyama et al. 2019) and is forming stars at a rate $\sim 0.02 - 0.1 M_{\odot} \text{ yr}^{-1}$, measured by counting numbers of young stellar objects or estimating the ionizing photon luminosity that trace recent star formation activity in a time period $\lesssim 10 \text{ Myr}$ (Yusef-Zadeh et al. 2009; Immer et al. 2012; Longmore et al. 2013; Koepferl et al. 2015). It has been noted that the observed SFR

in the CMZ is a factor of ~ 10 smaller than what is expected for its gas mass or column density (Longmore et al. 2013; Kruijssen et al. 2014). Using numerical simulations, Seo & Kim (2013) and Seo et al. (2019) showed that the ring SFR is closely related to the mass inflow rate to the ring rather than the ring mass, suggesting that the low current SFR of the CMZ is due to small mass inflow rates in the near past. Since this result can in principle depend on the treatment of star formation and feedback adopted in those works, it needs to be confirmed using new simulations with more realistic treatment of relevant physics in higher resolution. We note that there is observational evidence that the mass inflow rate to the CMZ varies considerably with time and currently has a very small value (Sormani & Barnes 2019).

As an alternative scenario, Kruijssen et al. (2014) proposed that the ring SFR undergoes quasi-periodic variations between starburst and quiescent phases, and the CMZ is currently in the quiescent phase (see also, Elmegreen 1994; Krumholz & Kruijssen 2015; Krumholz et al. 2017; Torrey et al. 2017; Armillotta et al. 2019). In this scenario, the inflowing gas gradually piles up until the ring becomes gravitationally unstable and undergoes intense star formation. Associated strong stellar feedback terminates the starburst phase rapidly, causing the ring to become quiescent until its mass grows sufficient to trigger another burst. Krumholz et al. (2017) ran numerical simulations based on vertically-integrated, axisymmetric, one-dimensional (1D) models and found that the ring SFR exhibits quasi-periodic oscillations with period ~ 20 Myr, even when the mass inflow rate is held constant.

However, it is questionable whether the quasi-periodic behavior of the ring SFR seen in the 1D models of Krumholz et al. (2017) exists in three-dimensional (3D) simulations for the CMZ (Armillotta et al. 2019; Tress et al. 2020; Sormani et al. 2020), or realized in observed galaxies. For instance, Armillotta et al. (2019) performed a global simulation of the Milky Way using GIZMO (Hopkins 2015). They modeled a stellar bar by a rigidly-rotating gravitational potential, and found that the ring SFR varies by more than an order of magnitude over a timespan of ~ 500 Myr, even though the gas mass in the CMZ stays relatively constant. While the short-period (~ 50 Myr) cycle in their ring SFR is likely modulated by feedback, the long-period (~ 200 Myr) cycle that dominates the SFR might be compromised by the orbital motions of a large molecular cloud which is unresolved and somehow survives in their simulation. Similar global simulations of Sormani et al. (2020) using AREPO (Springel 2010; Weinberger et al. 2020) found

that the gas depletion time in the CMZ is quite steady and that the SFR is directly proportional to the time-varying CMZ mass (see also Tress et al. 2020). The temporal changes of the CMZ mass and SFR in the models of Sormani et al. (2020) might be driven by the time variation in the mass inflow rate, as suggested by Seo et al. (2019).

Diverse results from the 3D simulations mentioned above imply that there is no consensus as to what controls the ring SFR, gas mass evolution, and detailed dynamical properties. In fully global simulations, the mass inflow rate is naturally time-variable since the gas density near the bar ends and along the dust lanes is highly inhomogeneous (e.g. Seo et al. 2019; Armillotta et al. 2019; Tress et al. 2020; Sormani et al. 2020). The time-dependent mass inflow rate causes the ring size, shape, and mass to vary significantly with time, making it difficult to isolate key factors that determine the ring SFR. For a more controlled study, in this paper we construct semi-global models that focus on a nuclear ring and nearby regions, without explicitly including a stellar bar in the simulations. Instead, our model have a stream of gas with prescribed properties entering through the domain boundaries, mimicking gas inflows along the dust lanes in global simulations (e.g., Athanassoula 1992; Kim et al. 2011b, 2012b; Sormani et al. 2015; Shin et al. 2017). We handle star formation and associated supernova (SN) feedback by adopting the Three-phase Interstellar medium in Galaxies Resolving Evolution with Star formation and Supernova feedback (TIGRESS) algorithms developed by Kim & Ostriker (2017). While our models cannot capture the triggering by the bar potential of large-scale gas inflows, they allow us to investigate the ring region itself with high resolution, and to explore the behavior of the ring SFR when the mass inflow rate is kept constant in time (at chosen levels).

Our semi-global models are also useful for investigating the details of star formation regulation in nuclear rings. Ostriker et al. (2010) and Ostriker & Shetty (2011) developed analytical equilibrium models for the self-regulation of SFR in normal and starburst regions of galactic disks, in which the equilibrium SFR is set by the balance between the weight of the interstellar medium (ISM) and the midplane pressure, with the required pressure provided primarily by SN feedback and far ultraviolet (FUV) heating. This equilibrium model has been validated through a series of local shearing-box simulations (Kim et al. 2011a, 2013; Kim & Ostriker 2015a), including spiral arms (Kim et al. 2020c), and for more extreme star-forming regions (Shetty & Ostriker 2012). In this work, we explore whether the self-

regulation theory is also applicable to the semi-global model of the galactic centers characterized by high SFRs and short dynamical timescales.

The remainder of this paper is organized as follows. In Section 2, we describe our numerical methods and our treatment of gas streams through the domain boundaries, and briefly summarize the TIGRESS framework for star formation and SN feedback. In Section 3, we present the temporal and morphological evolution of our models as well as the star formation histories. In Section 4, we present various physical quantities characterizing nuclear rings and explore their correlations, testing the self-regulation theory of star formation. Finally, we summarize and discuss our results in Section 5.

2. NUMERICAL METHODS

In this paper, we use the TIGRESS framework to study star formation and SN feedback in a nuclear ring located near a galaxy center. Ring formation is driven by stellar bars, which cause gas to flow radially inward while still retaining enough angular momentum to circularize at some distance from the galactic nucleus. In the present work we do not model the bar explicitly, instead imposing the gas inflows via boundary conditions (see below).

2.1. Basic Equations

Our simulation domain is a Cartesian cube with side length L , encompassing a nuclear ring. The simulation domain rotates at an angular frequency $\boldsymbol{\Omega}_p = \Omega_p \hat{\mathbf{z}}$, where this represents the pattern speed of a bar (on larger scale than we are simulating). The equations of hydrodynamics in the rotating frame read

$$\frac{\partial \rho}{\partial t} + \nabla \cdot (\rho \mathbf{v}) = 0, \quad (1)$$

$$\frac{\partial(\rho \mathbf{v})}{\partial t} + \nabla \cdot (\rho \mathbf{v} \mathbf{v} + P \mathbb{I}) = -2\rho \boldsymbol{\Omega}_p \times \mathbf{v} - \rho \nabla \Phi_{\text{tot}}, \quad (2)$$

$$\begin{aligned} \frac{\partial}{\partial t} \left(\frac{1}{2} \rho v^2 + \frac{P}{\gamma - 1} \right) + \nabla \cdot \left[\left(\frac{1}{2} \rho v^2 + \frac{\gamma P}{\gamma - 1} \right) \mathbf{v} \right] \\ = -\rho \mathbf{v} \cdot \nabla \Phi_{\text{tot}} - \rho \mathcal{L}, \end{aligned} \quad (3)$$

$$\nabla^2 \Phi_{\text{self}} = 4\pi G(\rho + \rho_{\text{sp}}), \quad (4)$$

where \mathbf{v} is the gas velocity in the rotating frame, P is the gas pressure, \mathbb{I} is the identity matrix, $\rho \mathcal{L}$ is the net cooling rate per unit volume, and $\Phi_{\text{tot}} = \Phi_{\text{cen}} + \Phi_{\text{ext}} + \Phi_{\text{self}}$ is the total gravitational potential, consisting of the centrifugal potential $\Phi_{\text{cen}} = -\frac{1}{2} \Omega_p^2 (x^2 + y^2)$, the exter-

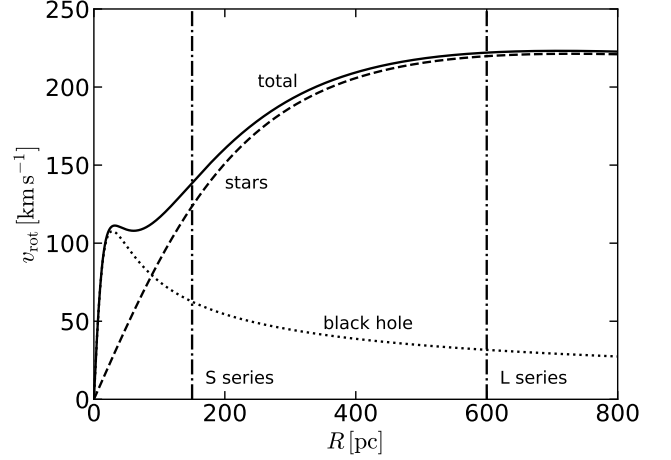


Figure 1. Rotation curve of our galaxy model. The solid line draws the circular velocity $v_{\text{rot}} = (Rd\Phi_b/dR + Rd\Phi_{\text{BH}}/dR)^{1/2}$, while the dashed and dotted lines show the individual contributions of Φ_b and Φ_{BH} to v_{rot} . Two vertical lines at $R_{\text{ring}} = 150$ pc and $R_{\text{ring}} = 600$ pc mark the ring positions in our S and L-series models, respectively.

nal gravitational potential Φ_{ext} giving rise to the background rotation curve, and the self-gravitational potential Φ_{self} of gas with density ρ and newly-formed star particles with density ρ_{sp} .

We adopt a model for the external potential based on the archetypal barred-spiral galaxy NGC 1097, which possesses a star-forming nuclear ring with radius of $R_{\text{ring}} \sim 700$ pc (Hsieh et al. 2011). Onishi et al. (2015) found that the observed gas kinematics near the galaxy center is consistent with the velocity field derived from the combined gravitational potential of stellar mass distribution and the supermassive black hole with mass $M_{\text{BH}} = 1.4 \times 10^8 M_{\odot}$, which we represent with a Plummer potential

$$\Phi_{\text{BH}} = -\frac{GM_{\text{BH}}}{\sqrt{r^2 + r_{\text{BH}}^2}}, \quad (5)$$

where $r_{\text{BH}} = 20$ pc is the softening radius. To represent stellar mass distribution, we use a modified Hubble profile with the stellar volume density

$$\rho_b = \frac{\rho_{b0}}{(1 + r^2/r_b^2)^{3/2}}, \quad (6)$$

and corresponding gravitational potential

$$\Phi_b = -\frac{4\pi G \rho_{b0} r_b^3}{r} \ln \left(\frac{r}{r_b} + \sqrt{1 + \frac{r^2}{r_b^2}} \right), \quad (7)$$

with $\rho_{b0} = 50 M_{\odot} \text{pc}^{-3}$ and $r_b = 250$ pc chosen so that the circular velocity at $r \sim 1$ kpc and shape at smaller scale are similar to the rotation curve for NGC 1097

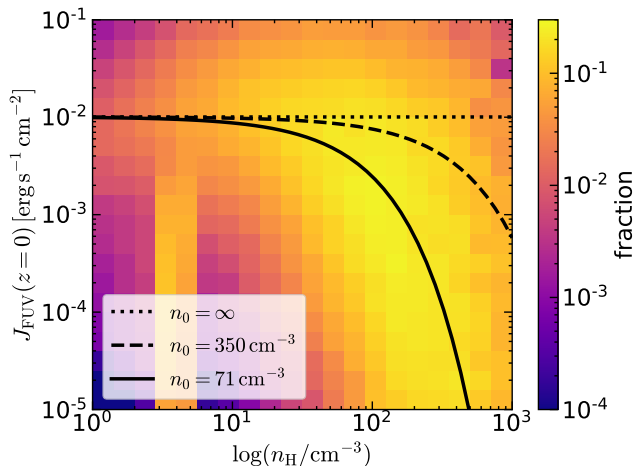


Figure 2. 2D histogram of J_{FUV} and n_{H} in the $z = 0$ plane, using our fiducial model. J_{FUV} is obtained by post-processing snapshots at $t = 100 - 110$ Myr, using the gas density distribution and locations and luminosities of all star particles, and employing the adaptive ray-tracing algorithm of Kim et al. (2017b). The dotted, dashed, and solid lines represent Equation (10) with $n_0 = \infty$, 350 cm^{-3} , and 71 cm^{-3} , respectively. Note that the vertical feature near $n_{\text{H}} = 4 \text{ cm}^{-3}$ is due to the gas along the inflowing streams.

from Onishi et al. (2015). Figure 1 shows the resulting rotation curve derived from $\Phi_{\text{ext}} = \Phi_{\text{b}} + \Phi_{\text{BH}}$.

The cooling rate in general depends on the chemical composition, ionization state, and temperature, while the heating rate depends on composition, electron abundance, and the radiation and cosmic ray energy densities. For the present work, in which we focus on dynamics rather than the exact thermal state, we adopt a simplified net cooling function $\rho\mathcal{L}$ in Equation (3) that consists of three parts:

$$\rho\mathcal{L} = n_{\text{H}}^2\Lambda - n_{\text{H}}\Gamma_{\text{PE}} - n_{\text{H}}\Gamma_{\text{CR}}. \quad (8)$$

Here $n_{\text{H}}^2\Lambda$ is the volumetric cooling rate, where $n_{\text{H}} = \rho/(1.4271m_{\text{H}})$ is the hydrogen number density assuming the solar abundances. We shall assume that Λ depends only on the gas temperature T , and use the fitting formula of Koyama & Inutsuka (2002, see also Kim et al. 2008) for $T < 10^{4.2}$ K, and the cooling function from Sutherland & Dopita (1993) for $T > 10^{4.2}$ K, where the latter is based on collisional ionization equilibrium at solar metallicity. The heating terms are $n_{\text{H}}\Gamma_{\text{PE}}$ representing the photoelectric heating rate by FUV radiation on dust grains, and $n_{\text{H}}\Gamma_{\text{CR}}$ representing the heating rate by cosmic ray (CR) ionization. For the equation of state $P = \rho k_{\text{B}}T/(\mu m_{\text{H}})$ with the Boltzmann constant k_{B} , we allow the mean molecular weight $\mu(T)$ to vary with T from $\mu_{\text{ato}} = 1.295$ for atomic gas to $\mu_{\text{ion}} = 0.618$ for ionized gas (see Kim & Ostriker 2017).

The main source of the FUV radiation is young massive stars, which in our simulations are a constant fraction of the mass of star cluster particles formed when gas collapses. In addition, we also allow for metagalactic FUV radiation. We therefore take the PE heating rate per hydrogen Γ_{PE} as

$$\Gamma_{\text{PE}} = \Gamma_{\text{PE},0} \left(\frac{\mu(T) - \mu_{\text{ion}}}{\mu_{\text{ato}} - \mu_{\text{ion}}} \right) \left(\frac{J_{\text{FUV}}}{J_{\text{FUV},0}} + 0.0024 \right), \quad (9)$$

where we take $\Gamma_{\text{PE},0} = 2 \times 10^{-26} \text{ erg s}^{-1}$ (Koyama & Inutsuka 2002) and $J_{\text{FUV},0} = 2.1 \times 10^{-4} \text{ erg s}^{-1} \text{ cm}^{-2} \text{ sr}^{-1}$ (Draine 1978) as normalizing factors based on solar neighborhood conditions. The term in the first parentheses in Equation (9) is to make the photoelectric heating completely shut off in the fully ionized gas. The small additional factor in the last parentheses in Equation (9) comes from the metagalactic radiation (Sternberg et al. 2002).

The FUV intensity would have large values in the regions near star particles and small values in deep inside clouds away from star particles due to dust attenuation. While it would be desirable to apply full radiative transfer to compute the FUV intensity $J_{\text{FUV}}(\mathbf{x}, t)$ throughout the domain, time-dependent ray-tracing from every star particle would be prohibitively expensive given the large ($\gtrsim 200$) number of sources in our simulations. Instead, we adopt a simpler and less computationally expensive approach. We calculate the total FUV luminosity \mathcal{L}_{FUV} of all star particles in the simulation domain (see Section 2.3) and use this to set the local J_{FUV} in a cell with density n_{H} according to

$$J_{\text{FUV}} = \frac{\mathcal{L}_{\text{FUV}}}{4\pi L^2} \left(\frac{1 - E_2(\tau_{\perp}/2)}{\tau_{\perp}} \right) e^{-n_{\text{H}}/n_0}. \quad (10)$$

Here $\tau_{\perp} = \kappa_{\text{d}}\Sigma$ with $\kappa_{\text{d}} = 10^3 \text{ cm}^2 \text{ g}^{-1}$ is the vertical optical depth for $\Sigma \equiv M_{\text{gas}}/L^2$ the average gas surface density, E_2 is the second exponential integral, and n_0 is a turnover density. M_{gas} is the total gas mass in the computational domain. The first two factors in Equation (10) corresponds to the solution of the radiation transfer equation in a plane-parallel geometry (see, e.g., Ostriker et al. 2010), while the exponential term takes into account the local shielding of FUV radiation inside dense clumps with $n_{\text{H}} \gtrsim n_0$.

To motivate Equation (10) and determine an appropriate value of n_0 for each of our models, we first run simulations by taking $n_0 = \infty$ (i.e., without FUV shielding) and select eleven snapshots during $100 \text{ Myr} \leq t \leq 110 \text{ Myr}$ after a nuclear ring already formed (see Section 3.1). We then post-process the snapshots by applying the adaptive ray-tracing algorithm developed by Kim et al. (2017b) to directly measure J_{FUV} produced

by all star particles. Figure 2 plots the normalized two-dimensional (2D) histogram of J_{FUV} and n_{H} in the mid-plane of our fiducial model (see below) at $t = 100\text{--}110$ Myr. The dotted, dashed, and solid lines draw Equation (10) with $n_0 = \infty$, 350 cm^{-3} , and 71 cm^{-3} , respectively, the last of which best describes $J_{\text{FUV}}(z = 0)$ resulting from the ray-tracing method. For each model we use the same procedure to compute n_0 ; Table 1 lists the adopted values obtained in this way. Overall, models with higher inflow rate and smaller ring size have higher gas density and thus larger n_0 .

In addition to photoelectric heating, we include CR heating which is responsible for heating the cold and dense gas for which photoelectric heating almost shuts off due to the exponential factor in Equation (10). We assume the CR heating rate is proportional to the SFR surface density Σ_{SFR} , also allowing for attenuation by a factor of Σ_0/Σ above a critical gas surface density $\Sigma_0 = 10.7 M_{\odot} \text{ pc}^{-2}$ (Neufeld & Wolfire 2017). We normalize by the CR heating rate and the SFR surface density in the solar neighborhood, $\Gamma_{\text{CR},0} = 3.2 \times 10^{-27} \text{ erg s}^{-1}$ and $\Sigma_{\text{SFR},0} = 3 \times 10^{-3} M_{\odot} \text{ yr}^{-1} \text{ kpc}^{-2}$ (Gong et al. 2017; Neufeld & Wolfire 2017). We thus have

$$\Gamma_{\text{CR}} = \Gamma_{\text{CR},0} \left(\frac{\mu(T) - \mu_{\text{ion}}}{\mu_{\text{ato}} - \mu_{\text{ion}}} \right) \frac{\Sigma_{\text{SFR}}}{\Sigma_{\text{SFR},0}} \min \left\{ 1, \frac{\Sigma_0}{\Sigma} \right\}, \quad (11)$$

where the factor in the parentheses shuts off CR heating by ionization in fully-ionized gas.¹

2.2. Gas Inflow Streams

In our simulations, the hydrodynamic effect of a non-axisymmetric bar is implemented via idealized gas streams originating on the y -boundaries, as depicted in Figure 3. We create the inflows via a pair of square-shaped nozzles each of size L_{in}^2 , offset by impact parameter b_{in} relative to the y -axis. The direction of the inflow velocity is inclined to the y -axis by angle θ_{in} to reflect that dust lanes are usually inclined relative to the bar semi-major axis (e.g., Comerón et al. 2009; Kim et al. 2012b).²

We vary the density ρ_{in} and speed v_{in} of the streams in order to control both the mass inflow rate \dot{M}_{in} and the ring radius R_{ring} that forms. From the condition that the specific angular momentum of the stream *in the inertial frame* is equal to that of circular ring consistent with the background rotation at radius $R = R_{\text{ring}}$, we

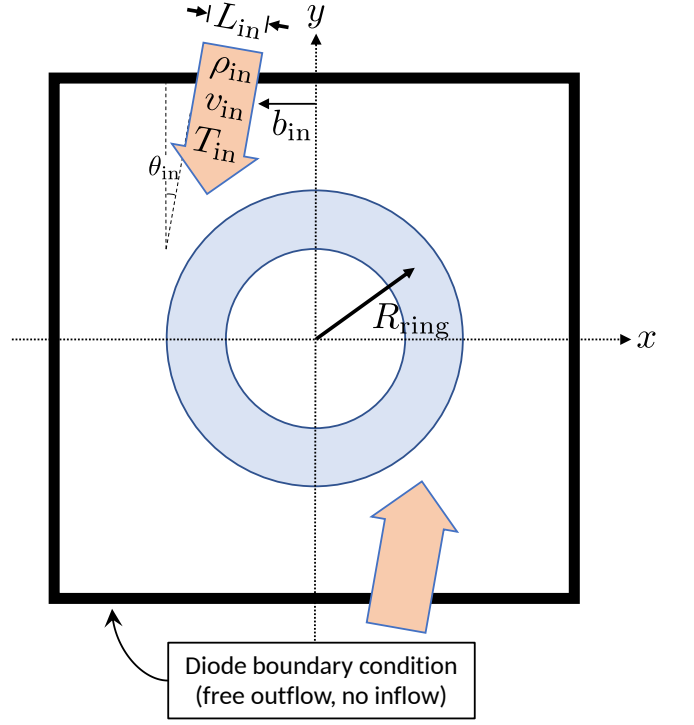


Figure 3. Schematic of the imposed gas inflows in our simulations, mimicking bar-driven inflows. Two gas streams flow into the computational domain through square-shaped nozzles with side L_{in} , located at the positive and negative y -boundaries (large arrows). $\theta_{\text{in}} = 10^\circ$ and b_{in} refer to the inclination angle and the impact parameter of the inflow stream relative to the y -axis. The blue shaded annulus represents the expected location for the ring formation. See text for details.

find

$$v_{\text{in}}(x, y) = \frac{R_{\text{ring}} v_{\text{rot}}(R_{\text{ring}}) - R^2 \Omega_p}{|x \cos \theta_{\text{in}} - y \sin \theta_{\text{in}}|}, \quad (12)$$

where $R = \sqrt{x^2 + y^2}$ is the galactocentric radius at the location of the nozzle. Note that v_{in} depends on x and y , indicating the inflow velocity varies across the nozzles; on the boundary $|y| = L/2$. The mass inflow rate is then given by

$$\dot{M}_{\text{in}} = 2 \int_{-L_{\text{in}}/2}^{L_{\text{in}}/2} \int_{b_{\text{in}}}^{b_{\text{in}}+L_{\text{in}}} \rho_{\text{in}} v_{\text{in}} \cos \theta_{\text{in}} dx dz. \quad (13)$$

For inflowing gas, we set the temperature to $T_{\text{in}} = 2 \times 10^4 \text{ K}$, which is typical of the warm neutral medium in our models. The choice of T_{in} is immaterial, however, because the temperature of the inflowing gas is quickly adjusted according to the heating and cooling rates once the stream enters the computational domain.

We caution the reader that if the simulation domain is large enough that $R^2 \Omega_p > R_{\text{ring}} v_{\text{rot}}(R_{\text{ring}})$ at the nozzles, it is not possible to choose a value for the inflow velocity consistent with a circular orbit at $R = R_{\text{ring}}$.

¹ In this work, we do not consider CR heating by scattering off free electrons in fully-ionized gas (e.g., Draine 2011).

² We find that gas streams escape the computational domain without forming a ring when θ_{in} is too small.

In this case, simple consideration of angular momentum conservation for ring formation is inadequate. Instead, it would be necessary to allow for a bar torque such that the inflowing gas can lose enough angular momentum to settle on a circular orbit at R_{ring} . For our idealized semi-global setup, the box size is therefore limited.

2.3. Star Particles and SN Feedback

A complete description for the creation and evolution of star particles and the prescription for treating supernovae can be found in [Kim & Ostriker \(2017\)](#). Here, we briefly summarize the key components. A cell undergoing gravitational collapse spawns a sink/star particle if the following three conditions hold simultaneously: (1) the gas density in the cell exceeds the Larson-Penston density threshold $\rho_{\text{LP}} = 8.86c_s^2/(G\Delta x^2)$, for grid spacing Δx ; (2) the cell lies at a local potential minimum; and (3) the velocity is converging in all three directions. A portion of the mass from a volume, $(3\Delta x)^3$, is removed from the grid and assigned to the sink particle upon creation. Each particle represents a star cluster that fully samples the [Kroupa \(2001\)](#) initial mass function (IMF). Particles act as sinks, accreting gas from their neighboring cells, until the onset of first SN explosion occurring at $t \sim 4$ Myr. The FUV luminosities of sink particles are assigned based on their mass and age using [STARBURST99 \(Leitherer et al. 1999\)](#) assuming a fully sampled Kroupa IMF.

For every sink particle with mass m_{sp} and mass-weighted mean age t_m , we estimate the expected number of supernova, $\mathcal{N}_{\text{SN}} = m_{\text{sp}}\xi_{\text{SN}}(t_m)\Delta t$, during hydrodynamic time step Δt , where $\xi_{\text{SN}}(t_m)$ is the SN rate tabulated in [STARBURST99](#). With our spatial resolution $\Delta x = 2$ pc or 4 pc, \mathcal{N}_{SN} is smaller than unity. We therefore turn on SN feedback only if $\mathcal{N}_{\text{SN}} > \mathcal{U}_{\text{SN}}$, where $\mathcal{U}_{\text{SN}} \in [0, 1)$ denotes a uniform random number.

Each supernova returns mass $M_{\text{ej}} = 10 M_{\odot}$, momentum, and energy to the neighboring cells. In the [TIGRESS](#) framework, the amount of momentum or energy injected depends on the local density and the resolution. If the ambient density is too high for the Sedov-Taylor stage to be resolved, we assume the remnant has already entered the snowplow phase and thus inject the expected final radial momentum $p_* = 2.8 \times 10^5 M_{\odot} \text{ km s}^{-1} (n_{\text{H}}/\text{cm}^{-3})^{-0.17}$ ([Kim & Ostriker 2015b](#)). If the density is sufficiently low such that the Sedov-Taylor stage is expected to be at least partially resolved, 72% of the total SN energy $E_{\text{SN}} = 10^{51}$ erg is injected as thermal energy, while the remaining 28% is injected as kinetic energy associated with the radial momentum. In our simulations, 80–90% of all SNe are resolved.

We follow the motion of sink particles by solving the equations of motion

$$\ddot{\mathbf{x}} = -\nabla\Phi_{\text{tot}} - 2\boldsymbol{\Omega}_p \times \dot{\mathbf{x}} \quad (14)$$

in the rotating frame. The original integrator used in [Kim & Ostriker \(2017\)](#) is for the equations of motion in a local shearing box and therefore inapplicable for our purpose. The usual explicit leap-frog integrator is also inappropriate, because it loses its symplectic nature in the presence of the velocity-dependent Coriolis force. Noting that the right hand side of Equation (14) has the same form as the Lorentz force in electromagnetism, we integrate Equation (14) using the Boris algorithm ([Boris 1970](#)), which is frequently adopted in kinetic codes for advancing charged particles under electromagnetic fields. In [Appendix A](#), we describe our implementation of the Boris algorithm and present a test result.

2.4. Models

We consider two series of models that differ in R_{ring} , the “target” size of the ring. The large ring models (L series) have $R_{\text{ring}} = 600$ pc, nozzle impact parameter $b_{\text{in}} = 320$ pc, and nozzle width $L_{\text{in}} = 200$ pc (see [Figure 3](#)). The L series models have domain size $L = 2048$ pc and number of cells per dimension $N = 512$, yielding grid spacing $\Delta x = L/N = 4$ pc. We construct small ring models (S series) by scaling down the L series by a factor of four, such that $R_{\text{ring}} = 150$ pc, $b_{\text{in}} = 80$ pc, $L_{\text{in}} = 50$ pc, and $L = 512$ pc. We take $N = 256$, corresponding to $\Delta x = 2$ pc, in order to mitigate a time step constraint arising from smaller cell size in the S series. For all models we adopt $\theta_{\text{in}} = 10^\circ$. For both series, we consider four different values for the inflow rate³, $\dot{M}_{\text{in}} = 1/8, 1/2, 2,$ and $8 M_{\odot} \text{ yr}^{-1}$. For the angular velocity of our computational domain, we take $\Omega_p = 36 \text{ km s}^{-1} \text{ kpc}^{-1}$, equal to the bar pattern speed in [NGC 1097 \(Piñol-Ferrer et al. 2014\)](#).

[Table 1](#) lists the parameters of all models. Column (1) gives the model name. Column (2) and (3) give R_{ring} and the bulge stellar density ρ_b at R_{ring} , respectively. Columns (4) and (5) give $n_{\text{H,in}} = \rho_{\text{in}}/(1.4271m_{\text{H}})$, and \dot{M}_{in} , respectively. Column (6) gives the mean inflow velocity $\bar{v}_{\text{in}} \equiv \dot{M}_{\text{in}}/(2\rho_{\text{in}}L_{\text{in}}^2 \cos \theta_{\text{in}})$. Columns (7) and (8) list the circular velocity $v_{\text{cir}} = v_{\text{rot}}(R_{\text{ring}}) - R_{\text{ring}}\Omega_p$ and the orbital period $t_{\text{orb}} = 2\pi R_{\text{ring}}/v_{\text{cir}}$ of the ring in the rotating frame, respectively. The circular velocity in the inertial frame is 222 km s^{-1} and 138 km s^{-1} for L and

³ As long as \dot{M}_{in} is fixed, different combinations of ρ_{in} and L_{in} does not lead to any noticeable differences on the ring properties.

Table 1. Model parameters

Model	R_{ring} (pc)	$\rho_b(R_{\text{ring}})$ ($M_{\odot} \text{ pc}^{-3}$)	$n_{\text{H,in}}$ (cm^{-3})	\dot{M}_{in} ($M_{\odot} \text{ yr}^{-1}$)	\bar{v}_{in} (km s^{-1})	v_{cir} (km s^{-1})	t_{orb} (Myr)	n_0 (cm^{-3})
(1)	(2)	(3)	(4)	(5)	(6)	(7)	(8)	(9)
L0	600	2.84	0.286	0.125	154	200	18.4	18
L1	600	2.84	1.15	0.5	154	200	18.4	35
L2*	600	2.84	4.58	2	154	200	18.4	71
L3	600	2.84	18.3	8	154	200	18.4	142
S0	150	31.5	5.71	0.125	123	133	6.92	71
S1	150	31.5	22.8	0.5	123	133	6.92	142
S2	150	31.5	91.3	2	123	133	6.92	283
S3	150	31.5	365	8	123	133	6.92	567

* Fiducial model.

S series, respectively. Column (9) gives the value of n_0 we take for the dust attenuation (see Equation 10). We take model L2 with $R_{\text{ring}} = 600 \text{ pc}$ and $\dot{M}_{\text{in}} = 2 M_{\odot} \text{ yr}^{-1}$ as our fiducial model.

The initial condition of our models is near-vacuum, filled with rarefied gas with $n_{\text{H}} = 10^{-5} \exp[-|z|/(50 \text{ pc})] \text{ cm}^{-3}$ and $T = 2 \times 10^4 \text{ K}$, rotating at $\mathbf{v} = \sqrt{R(\partial\Phi_{\text{tot}}/(\partial R))} \hat{\phi}$. The subsequent evolution is governed entirely by the mass inflow from the boundaries.

We integrate Equations (1)–(4) using a modified version of the *Athena* code (Stone et al. 2008), which solves the equations of hydrodynamics or magnetohydrodynamics using finite-volume Godunov methods. In the present work, we do not include magnetic fields. Our simulations use the van Leer integrator (Stone & Gardiner 2009), Roe’s Riemann solver with H-correction (Sanders et al. 1998), and second-order spatial reconstruction. When needed, we apply first-order flux correction (Lemaster & Stone 2009). We solve the Poisson equation via FFT convolution with open boundary conditions (Skinner & Ostriker 2015); the density of star particles is included using a particle-mesh approach as in Kim & Ostriker (2017).

Within the nozzle region on the boundaries, we apply inflow boundary conditions as described in Section 2.2. For the rest of the boundaries, we take diode boundary conditions: we extrapolate the hydrodynamic variables from the last two active zones to the ghost cells, and set the normal velocity to zero if the gas is inflowing. This allows gas to freely escape from the computational domain, while ensuring no inflow occurs except through the nozzles.

3. EVOLUTION

In this section, we describe overall temporal and morphological evolution of our fiducial model, focusing on ring formation, star formation histories, and distributions of gas and star particles. Steady-state physical quantities averaged over the nuclear ring and their correlations will be presented in Section 4.

3.1. Overall Evolution of the Fiducial Model

Figures 4 and 5 provide a visual impression of overall time evolution of model L2, in the x - y plane and x - z plane, respectively.

At early time, the gas streams injected through the nozzles closely follow the ballistic orbits shown as gray solid lines in the leftmost top panel. Orbit crowding, as manifested by convergence of the ballistic orbits near $(x, y) = (\pm 0.3, \pm 0.2) \text{ kpc}$, triggers the first star formation in the inflowing streams at $t = 5.1 \text{ Myr}$.

In about a half of the (rotating-frame) orbital time $t_{\text{orb}}/2 = 9.2 \text{ Myr}$, the two inflowing streams start to collide with each other and produce strong shocks with Mach number of ~ 15 . Star formation then begins at the contact points where the inflowing streams collide. The sink particles produced at very early time have highly eccentric orbits close to the ballistic orbits of the streams and thus most of them leave the computational domain. SN feedback from these particles (prior to their escape) produces hot gas that fills most of the volume, inside and outside the gas streams.

Unlike the early sink particles, however, gas loses a significant amount of kinetic energy at every passage of the contact points and orbits become less eccentric, eventually creating a ring-like shape. While star-forming regions are concentrated near the contact points at early

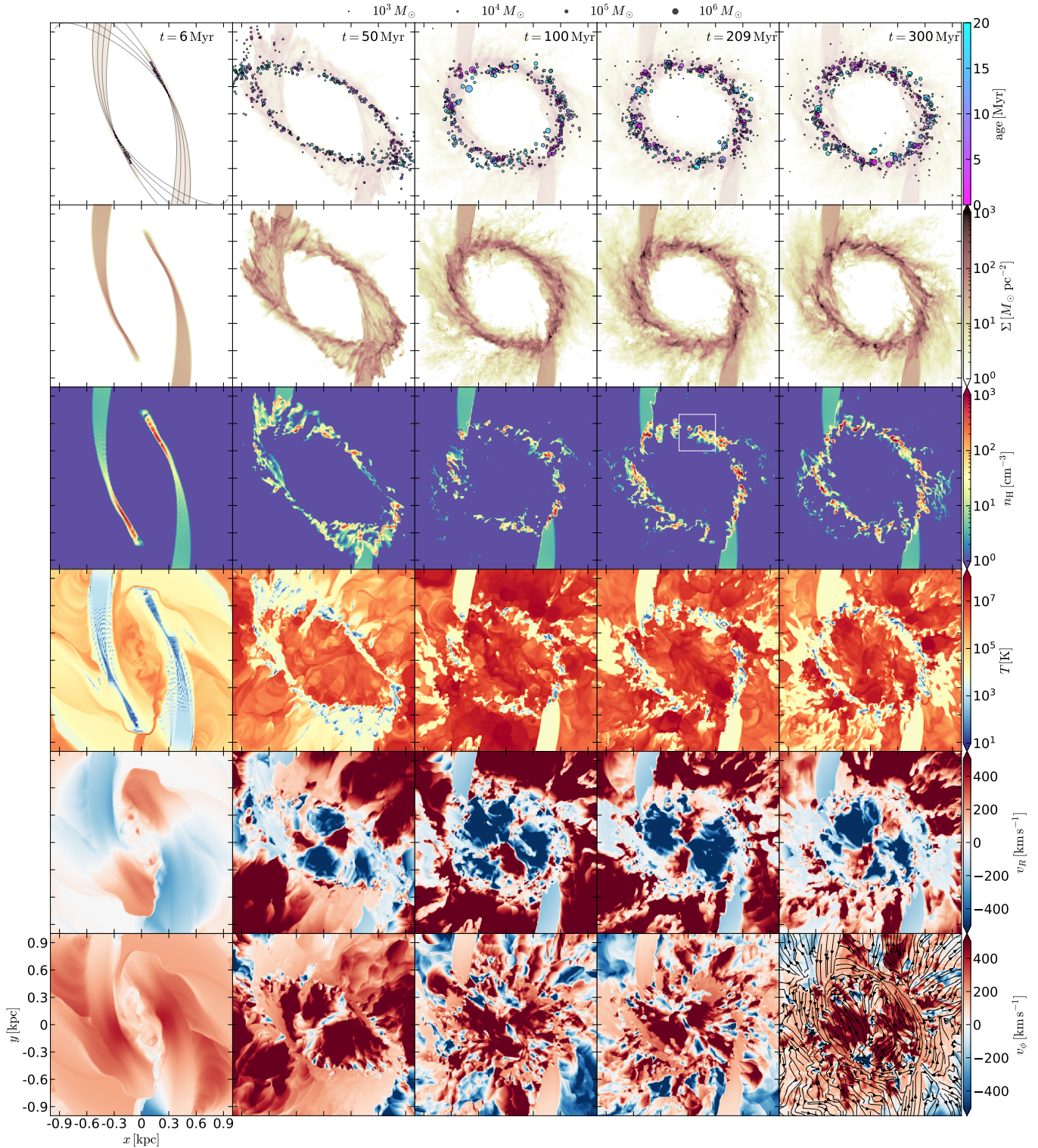


Figure 4. Face-on views of model L2 at $t = 6, 50, 100, 209, 300$ Myr (columns from left to right). From top to bottom, rows display: the projected positions of sink particles, integrated gas surface density Σ , hydrogen number density n_{H} , temperature T , radial velocity v_R , and azimuthal velocity v_ϕ in the rotating frame. The last four rows show slices through $z = 0$. In the top row, Σ is also shown in the background for reference. The gray solid lines in the leftmost top panel draw the expected orbits of pressureless particles injected at the nozzles. The white square box in the fourth panel of the third row marks the zoom-in region shown in Figure 7. The black solid lines with arrows in the rightmost bottom panel plot the gas streamlines at the midplane. Gas streams injected from the nozzles initially follow ballistic orbits, colliding with the stream from the opposite side at $t \sim 8.5$ Myr. The collision drives strong shocks which gradually remove the kinetic energy from the gas streams. Eventually, gas settles down to a roughly circular orbit and forms a nuclear ring with radius $R \approx 600$ pc.

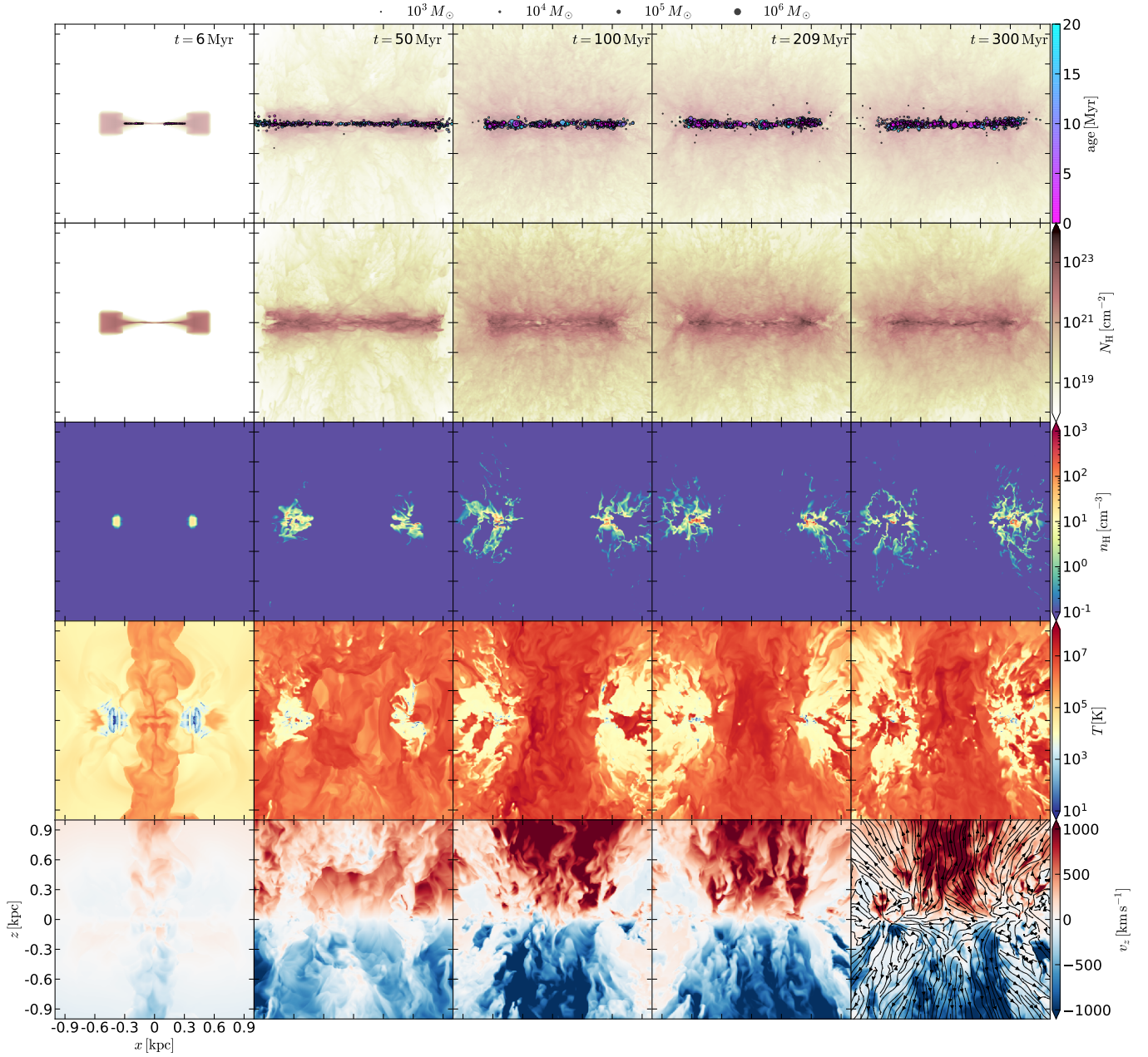


Figure 5. Edge-on views of model L2 at $t = 6, 50, 100, 209, 300 \text{ Myr}$ (columns from left to right). From top to bottom, rows display: the projected positions of the sink particles, hydrogen column density $N_{\text{H}} = \int n_{\text{H}} dy$, hydrogen volume density n_{H} , temperature T , and vertical velocity v_z . The last three rows show slices through $y = 0$. The black solid lines with arrows in the rightmost bottom panel plot the gas streamlines. Superbubbles produced by interactions of multiple SN explosions lead to persistent winds.

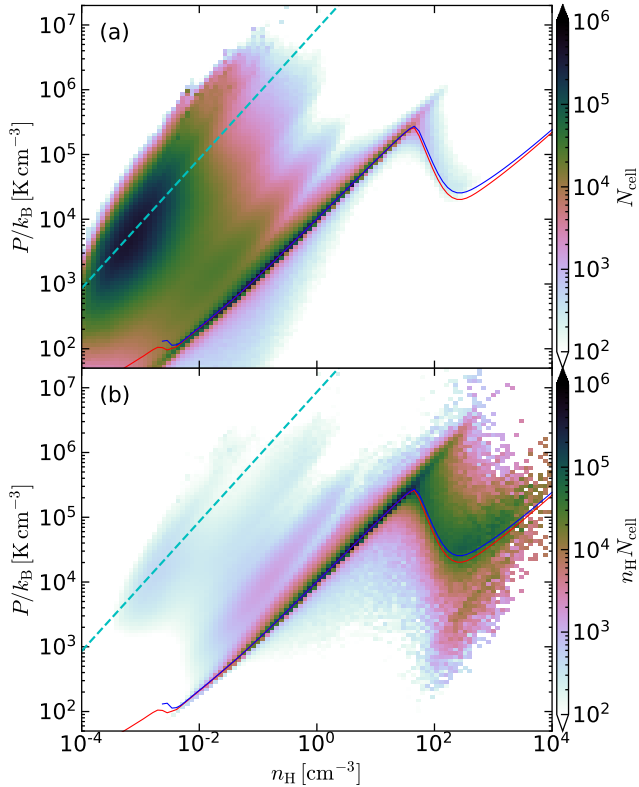


Figure 6. (a) Volume- and (b) density-weighted joint PDF in P/k_B and n_H of model L2 at $t = 250$ Myr. The red line is the thermal equilibrium curve under the instantaneous radiative heating rate at that epoch, while the blue line corresponds to an equilibrium curve with additional turbulent heating rate Γ_{turb} (see text), which yields slightly better agreement with the mean PDFs. Most of the warm and cold medium follows the blue line, with some scatter due to intermittent shock heating. The dashed line indicates the mean temperature $T = 3.7 \times 10^6$ K of the hot medium.

time, they soon become widely distributed as strong SN feedback makes the ring highly clumpy everywhere, enabling local collapse. At $t \sim 100$ Myr, the system reaches a quasi-steady state in which the ring morphology and various statistical quantities including the ring gas mass and SFR do not change appreciably over time. The radius of the nuclear ring is $R \sim 600$ pc in model L2, consistent with the expectation from the angular momentum conservation (Equation 12). For the fiducial model, the in-plane width of the gas ring is ~ 200 pc. After steady state is reached, the star formation in model L2 (and other models) is not concentrated in preferred regions of the ring but occurs randomly in space and time. The star formation/feedback cycle does not have strong bursts (from either spatial or temporal correlations in gas collapse). As a result, the steady inflow rate adopted in our models gives rise to a steady SFR with small temporal fluctuations for model L2 (and other

models). SN feedback never destroys the ring completely in model L2 as shown in Figure 4. We find that our models generally show the steady star formation and persistence of the ring.

SN feedback as well as gravitational and thermal instabilities produce cold and dense cloudlets distributed around the nuclear ring. Figure 6 display the volume- and mass-weighted probability distribution functions (PDFs) of n_H and P/k_B at $t = 250$ Myr. The volume fractions of the hot ($T > 2 \times 10^4$ K) and the cold-warm ($T < 2 \times 10^4$ K) phases are 84% and 16%, while their mass fractions are 2% and 98%, respectively.

The mean thermal pressure of the cold-unstable medium with $T < 5050$ K is somewhat enhanced above the equilibrium curve with the instantaneous total heating rate at that epoch, shown as the red line. This enhancement is observed in all epochs, suggesting that it is not caused by chance due to fluctuation of heating rate. Instead, this enhanced pressure (or temperature) may be attributed to dissipation of (turbulent) kinetic energy in the ring. To get a rough estimate of the kinetic energy dissipation rate due to (marginally-resolved) cloud-scale turbulence, we calculate the mass-weighted vertical velocity dispersion $\sigma_z \sim 12$ km s $^{-1}$ and the scale height $H \sim 26$ pc of the cold-unstable medium, and estimate the turbulent heating rate (per hydrogen) as $\Gamma_{\text{turb}} = \frac{3}{2} \mu_H m_H \sigma_z^3 / H$. The blue line shows the equilibrium curve when Γ_{turb} is additionally included, showing a slightly better agreement with the PDFs for the cold-unstable medium. At $n_H = 10^3$ cm $^{-3}$, the heating rates due to FUV, CR, and (assumed) turbulent dissipation are $\Gamma_{\text{PE}} = 5.8 \times 10^{-5} \Gamma_{\text{PE},0}$, $\Gamma_{\text{CR}} = 6.2 \Gamma_{\text{PE},0}$, and $\Gamma_{\text{turb}} = 3.9 \Gamma_{\text{PE},0}$, respectively. We note that actual kinetic energy dissipation rate might be even larger than Γ_{turb} considering numerical dissipation. Although our treatment of the FUV and CR heating is rather simplified, the above result suggests that the turbulent heating could be a major heating source for the dense gas where the radiation is heavily shielded (e.g., Ginsburg et al. 2016).

Figure 5 shows that most of the star formation takes place in the high-density gas near the midplane, while the distribution of lower-density gas extends vertically up to $|z| \sim 500$ pc due to SN feedback. For example, at $t = 300$ Myr (last column) there are three large bubbles centered at $(x, z) \sim (-700$ pc, 150 pc), $\sim (-500$ pc, 100 pc), and $\sim (-800$ pc, -150 pc) in the negative- x portions of the ring, that lift up the gas to high latitude. Heated by the SN shocks, gas inside the bubbles reaches $\sim 10^7$ K. Sometimes the hot gas inside the superbubbles breaks out through the cold-warm medium, such as the bubble at $(x, z) \sim$

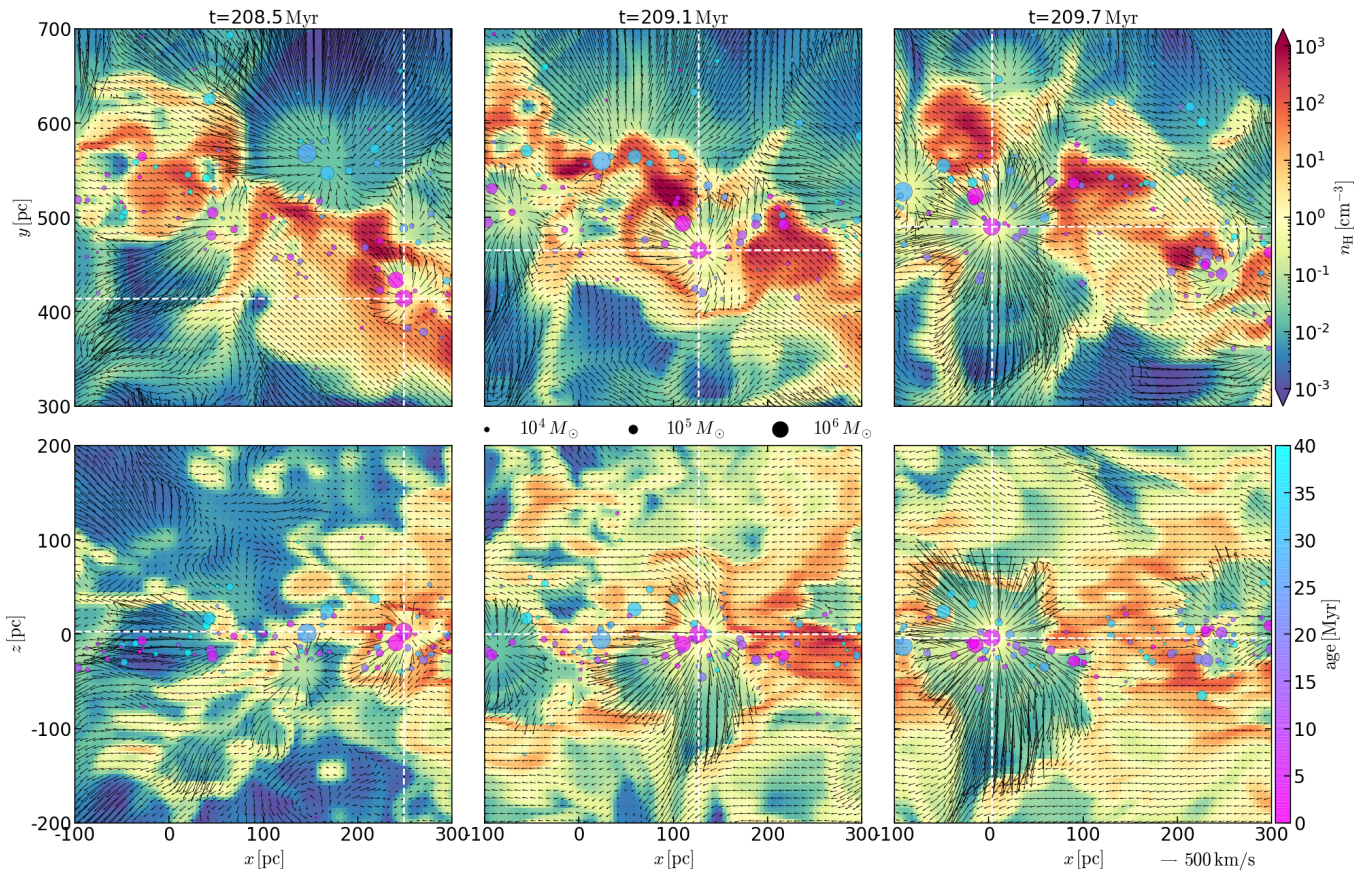


Figure 7. Close-up view of the ring: three consecutive snapshots of model L2 at $t = 208.5, 209.1, 209.7$ Myr from left to right. The top panels show the density and velocities (v_x, v_y) in the $z = 0$ plane at $-0.1 \text{ kpc} \leq x \leq 0.3 \text{ kpc}$ and $0.3 \text{ kpc} \leq y \leq 0.7 \text{ kpc}$. Also shown are sink particles within $|z| \leq 0.2 \text{ kpc}$. Vertical and horizontal dashed lines trace the location of a selected sink particle, which moves over a few 100 pc within a few Myr, due to its orbital motion (including epicyclic oscillations). The bottom panels show the density and velocities (v_x, v_z) at $y = 0.41, 0.47, 0.49$ kpc, corresponding to the y coordinates of the selected sink particle in the top panels. Other sink particles from the top panels are also shown. Arrows show the velocity field, where the arrow length is proportional to the velocity magnitude in x - y (top panels) and x - z (bottom panels) plane.

($-800 \text{ pc}, -150 \text{ pc}$). Away from the midplane the hot gas dominates.

Superbubbles created by repeated feedback from relatively young cluster particles typically have a diameter of $\sim (100 - 200) \text{ pc}$, comparable to the ring width of $\sim 200 \text{ pc}$, so that a fraction of the feedback energy and momentum escape from the ring through the holes like champagne flows. This is illustrated in Figure 7 which displays the density and velocity fields as well as star particles with age less than 40 Myr in a zoomed-in region within the ring for model L2 at $t = 208.5, 209.1, 209.6$ Myr. A superbubble surrounding the star particle with $(x, y) = (250, 410) \text{ pc}$ at $t = 208.5$ Myr expands and blows out, dispersing a part of the ring and compressing the gas nearby, as the particle moves to $(x, y) = (3, 466) \text{ pc}$ at $t = 209.7$ Myr. Since orbits of star particles deviate from that of the gas, relatively old particles can explode in the regions outside the ring. For instance, the clusters near $(x, y) = (150, 570) \text{ pc}$ at

$t = 208.5$ Myr are located near the outer edge of the ring. In this case, only a small fraction of the feedback energy contributes to turbulence in the ring material. Because the ring gas is quite spatially confined in radial direction and the gas and stellar orbits differ, much of the feedback energy is transferred to the gas outside the star-forming ring, resulting in lower feedback yield to cold-warm gas than in previous simulations with more uniform distribution of gas in the horizontal direction (see discussion in Section 4.2).

Hot gas created by individual SN shocks merges together to launch large, coherent outflows resembling galactic winds. These quasi-conical outflows are clearly visible in the bottom row of Figure 5. For the same model, Figure 8(a) plots in the x - z plane gas streamlines overlaid over the thermal pressure. For these streamlines, we average over $t = 200 - 300$ Myr and include all of the gas in the $y = 0$ slice. The ring shows up like bull's-eyes at $|x| \sim 600 \text{ pc}$ in the pressure map, from

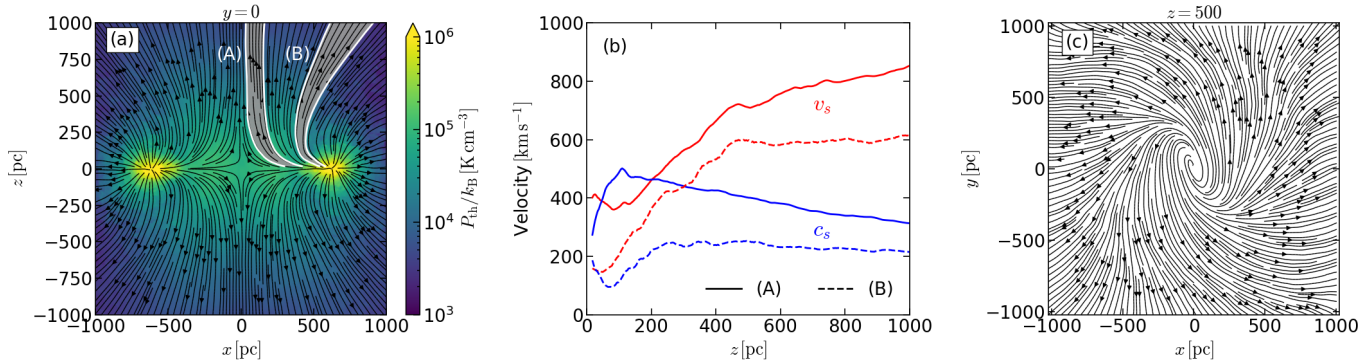


Figure 8. (a) Gas streamlines in model L2 overlaid over the thermal pressure in the x - z plane averaged over $t = 200$ to 300 Myr. The ring appears as bull’s-eyes at $|x| \sim 600$ pc. Streamlines emerge from the ring due to the SN feedback and lead to large-scale hot superwinds. (b) Vertical profile of the poloidal velocity $\langle v_s \rangle \equiv (\langle v_R \rangle^2 + \langle v_z \rangle^2)^{1/2}$ (red) and the sound speed $\langle c_s \rangle$ (blue) along the selected streamlines (A) and (B) shown in (a). (c) Time-averaged streamlines in the x - y plane at $z = 500$ pc, showing the helical wind.

which the streamlines emerge. Figure 8(b) plots the vertical profiles of the time-averaged poloidal velocities and the sound speed of the gas along the selected streamlines shown in Figure 8(a). It is apparent that the wind is accelerated beyond the sonic point, readily reaching $\approx (600 - 900) \text{ km s}^{-1}$ at $z = 1 \text{ kpc}$. Figure 8(c) plots the time-averaged streamlines at $z = 500$ pc, showing that the winds are helical, with the rotational velocity decreasing as gas moves outward radially conserving angular momentum.

We note that the subsonic to supersonic transition of the winds was absent in the previous local simulations in which the streamlines cannot open up due to the combination of a relatively small box and SNe throughout the midplane region (e.g., Martizzi et al. 2016; Kim & Ostriker 2018). Here, the relatively small size of the star-forming ring within the domain allows streamlines to open up, leading to the characteristic bi-conical shape and supersonic transition often seen in both observations (Strickland et al. 2004; Yukita et al. 2012) and simulations (Wada et al. 2009; Fielding et al. 2017; Schneider et al. 2018). We note that in contrast to previous simulations of central starburst-driven winds where the locations of SN feedback were imposed by hand, here the SN location distribution arises naturally from star formation within the ring.

3.2. Star Formation

Figure 9(a) plots the temporal evolution of the total mass in the gas M_{gas} and in the sink particles M_{sp} in model L2. The total gas mass saturates to $M_{\text{gas}} \sim 8.5 \times 10^7 M_{\odot}$ within $\sim 3t_{\text{orb}}$, while M_{sp} steadily increases with time, except for the initial phase when stars formed in the inflowing streams escape from the computational box.

Figure 9(b) plots the mass inflow rate \dot{M}_{in} to the box, outflow rate \dot{M}_{out} from the box, and deposition rate \dot{M}_{ej} from SN ejecta in model L2. The mass inflow rate is fixed to $\dot{M}_{\text{in}} = 2 M_{\odot} \text{ yr}^{-1}$ at the nozzles, and $\dot{M}_{\text{ej}} \sim 0.2 M_{\odot} \text{ yr}^{-1}$ is roughly constant after $t = 100$ Myr when the SFR reaches a quasi-steady state. The mass outflow rate through the domain boundaries is quite large at early time ($t \lesssim 30$ Myr) due to the gas leaving the domain through the y -boundaries before gas orbits are circularized (Figure 4). Except for these early transients, \dot{M}_{out} is dominated by SN-driven outflows and saturates to $\sim 0.67 M_{\odot} \text{ yr}^{-1}$ with some fluctuations.

We calculate the SFR at time t by

$$\dot{M}_{\text{SF}}(t, \Delta t) = \frac{M_{\text{sp}}(t) - M_{\text{sp}}(t - \Delta t)}{\Delta t}, \quad (15)$$

where Δt is a chosen time window for averaging. We take $\Delta t = 1, 10, \text{ or } 40$ Myr to allow for different timescales pertinent to common observational tracers of the SFR (see, e.g., Kennicutt & Evans 2012): $\Delta t = 1$ Myr corresponds to the *instantaneous* SFR, while $\Delta t = 10$ and 40 Myr are appropriate for H α and radio free-free/recombination lines, or to FUV/IR tracers, respectively. Figure 9(c) and (d) plot \dot{M}_{SF} and the gas depletion time $t_{\text{dep}} \equiv M_{\text{gas}}/\dot{M}_{\text{SF}}$, respectively. At early time, the SFR is lower than the inflow rate and gas builds up in the ring, increasing M_{gas} eligible for star formation. The SFR increases with time until the system enters a quasi-steady state. In model L2, the steady-state SFR is $\dot{M}_{\text{SF}} \sim 1.66 M_{\odot} \text{ yr}^{-1}$, corresponding to 83% of \dot{M}_{in} . The average depletion time after a steady-state is reached is $t_{\text{dep}} = 51.2$ Myr.

While the mean values of the SFR is insensitive to Δt , temporal fluctuations decrease with Δt . Fluctuation amplitudes are $0.55, 0.28, \text{ and } 0.09 M_{\odot} \text{ yr}^{-1}$ for $\Delta t = 1, 10, \text{ and } 40$ Myr, respectively. Our simulations

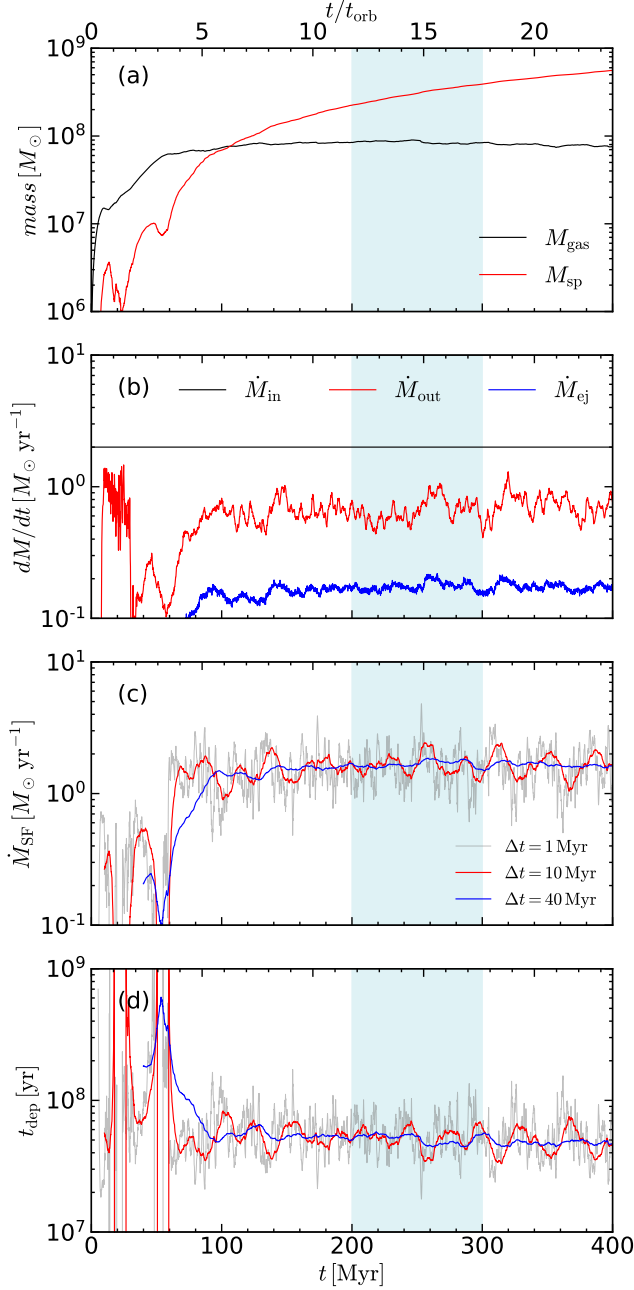


Figure 9. Temporal history in model L2 of (a) the total gas mass (M_{gas} ; black), the total mass of the sink particles representing star clusters (M_{sp} ; red), (b) the mass inflow rate (\dot{M}_{in} ; gray) through the nozzles, the mass outflow rate (\dot{M}_{out} ; red) through the domain boundaries, and the rate of the mass return from SN feedback (\dot{M}_{ej} ; blue), (c) the SFR averaged over $\Delta t = 1$ Myr (gray), $\Delta t = 10$ Myr (red), and 40 Myr (blue), and (d) the gas depletion time $t_{\text{dep}} = M_{\text{gas}}/\dot{M}_{\text{SF}}$ within the domain. The mean gas mass, SFR, and the depletion time in the shaded region ($200 \text{ Myr} \leq t \leq 300 \text{ Myr}$) are $8.5 \times 10^7 M_{\odot}$, $1.7 M_{\odot} \text{ yr}^{-1}$, and 51.2 Myr, respectively.

do not exhibit a burst/quench cycle as seen in the model of Krumholz et al. (2017) and simulation of Torrey et al. (2017), nor the long-term variation in the depletion time seen in Armillotta et al. (2019) (who found a range $t_{\text{dep}} \sim 10^8 - 10^9 \text{ yr}$). More similar to our results were those of Sormani et al. (2020), who ran moving-mesh simulations with star formation and feedback targeting star formation in the CMZ, and found that the SFR and the depletion time are quite steady with time, with only modest (within factor two) variations. Our results suggest that under a constant inflow rate, the SFR in nuclear rings would be quite steady. This would also imply that bursty behavior in real systems is due to variations in the feeding rate from larger scales. We shall compare the numerical results with the prediction of the self-regulation theory (Ostriker et al. 2010; Ostriker & Shetty 2011) in Section 4.2.

3.3. Other Models

Evolution of the other models is qualitatively similar to that of the fiducial model, although the ring size and shape, SFR, etc. depend significantly on the model parameters R_{ring} and \dot{M}_{in} . Figure 10 compares distributions in the x - y plane of gas and sink particles for all the models at $t = 250$ Myr, after a steady-state is reached. The left and right columns correspond to the L and S series, respectively, with increasing \dot{M}_{in} from top to bottom. In both series, the mean surface density of the ring Σ_{ring} and its ellipticity increase with \dot{M}_{in} . The increase of Σ_{ring} with \dot{M}_{in} is because the associated higher SFR yields larger thermal and turbulent pressures via feedback that support the ring against stronger gravity (see Section 4.2). At higher SFR, gas turns into stars before the inflowing streams are fully circularized, yielding a more eccentric ring. Rings in the S series are overall more eccentric compared to their counterparts in the L series. This is because the ratio $t_{\text{dep}}/t_{\text{orb}}$ is smaller in the S series, implying that more gas is consumed by star formation before the orbit circularization. We note that some barred galaxies including NGC 986, NGC 1365, NGC 3351, and NGC 5383 possess an eccentric nuclear ring at their centers, similarly to our models with a high inflow rate.

Figure 10 shows that the masses of individual sink particles, on average, increase with \dot{M}_{in} due to the increase of Σ_{ring} . Because sink particles inherit the gas velocity from which they form, their initial orbits are eccentric, similarly to the gas ring. Unlike the gas, however, the sink particles do not suffer direct collisions at the contact points and their orbits freely precess under the total gravitational potential. As a result, the spatial distribution of the sink particles deviates from that

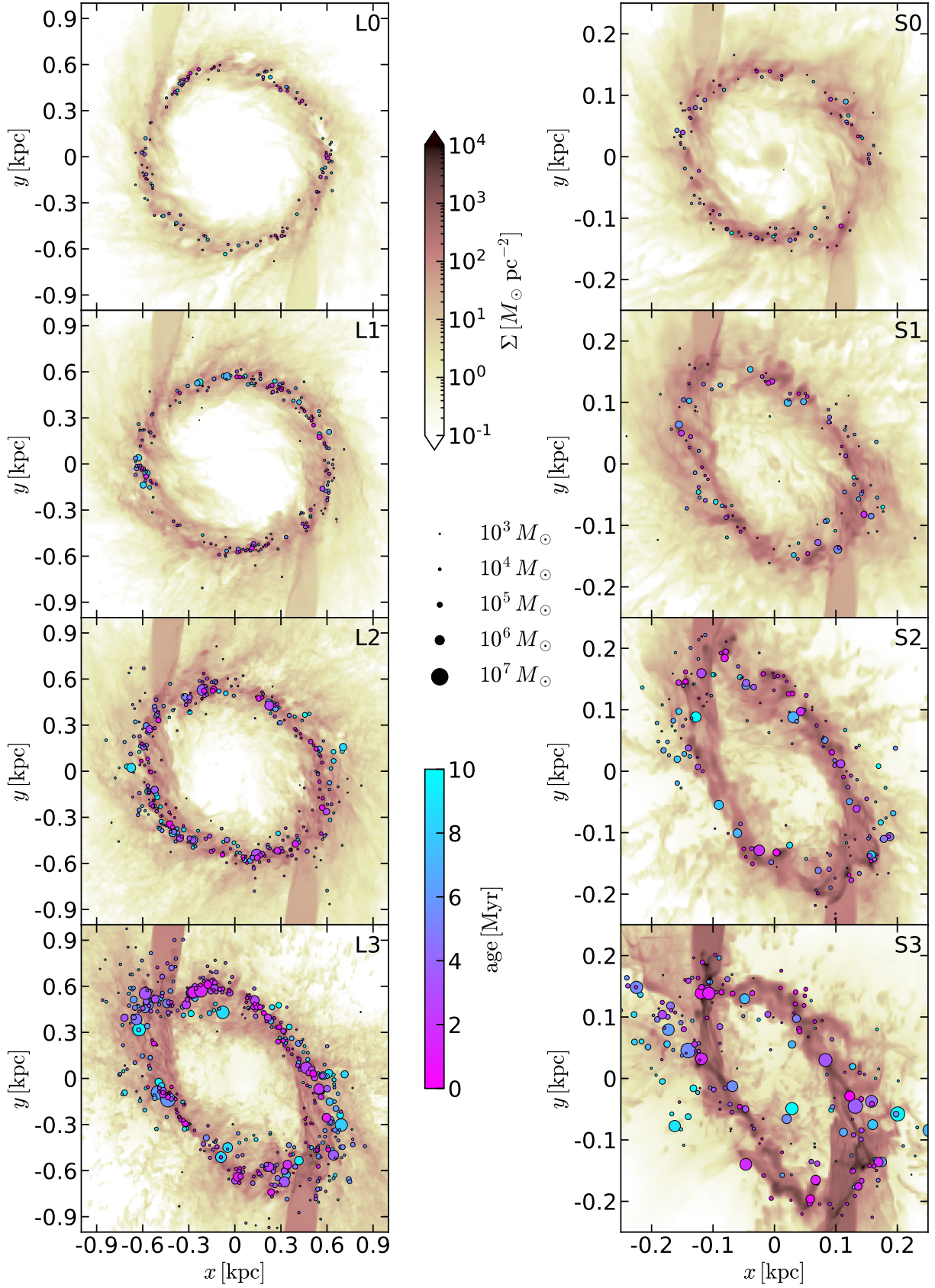


Figure 10. Distributions of the gas surface density Σ and sink particles with age less than 10 Myr, for all models at $t = 250$ Myr. The left and right columns are for the L and S series, respectively (note difference in box size). From top to bottom, rows correspond to the models with $\dot{M}_{\text{in}} = 0.125, 0.5, 2, \text{ and } 8 M_{\odot} \text{ yr}^{-1}$. All panels share the same color scale for Σ and the same symbol size and color scale for star particle mass and age, given in the middle.

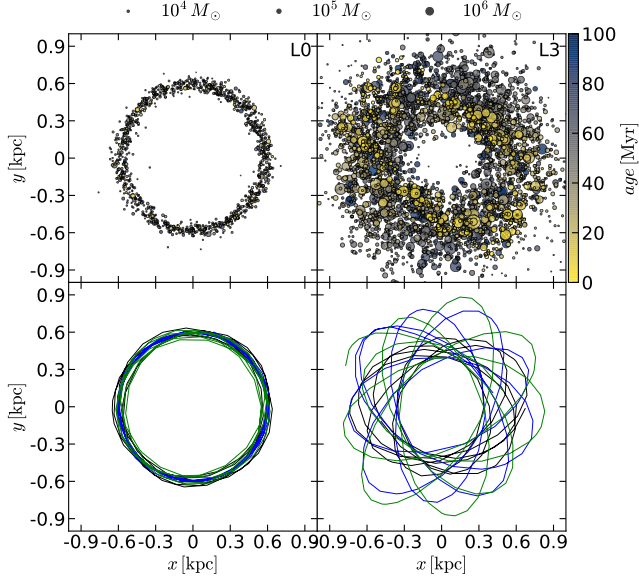


Figure 11. *Top:* Spatial distributions of sink particles younger than 100 Myr at $t = 300$ Myr for models L0 (left) and L3 (right). *Bottom:* Representative trajectories of some sink particles during $t = 200$ –300 Myr.

of the gas. The deviation is more prominent in models with larger \dot{M}_{in} due to more eccentric orbits of the sink particles.

Figure 11 compares the projected distributions of sink particles and their orbits in the x - y planes between models L0 and L3. Since the ring is almost circular in model L0, the orbits of the sink particles are also nearly circular. Consequently, both the gas and the sink particles form a narrow circular annulus near R_{ring} . In model L3, however, the orbits of the sink particles have high eccentricities and precess. As they age, they diffuse out of the gaseous ring and also precess, occupying a much wider range of radius. Young particles with $t_m \lesssim 10$ Myr are still found quite close to the eccentric gaseous ring for model L3. While our simple sink particles retain their individual identities, in reality the older massive clusters could be disrupted (de Grijs & Anders 2012; Väisänen et al. 2014) and form a pseudobulge (Kormendy & Kenicutt 2004).

In our simulations, the cold-warm gas with $T < 2 \times 10^4$ K comprises about 98% of the total mass. To quantify the physical properties of the cold-warm gas in our simulations, we compute the midplane values of the mass-weighted turbulent velocity dispersion σ_z and sound speed c_s , and also measure the scale height H , via

$$\sigma_z = \left(\frac{\iint_{z=-\Delta z}^{z=\Delta z} \rho v_z^2 \Theta \, dx dy dz}{\iint_{z=-\Delta z}^{z=\Delta z} \rho \Theta \, dx dy dz} \right)^{1/2}, \quad (16)$$

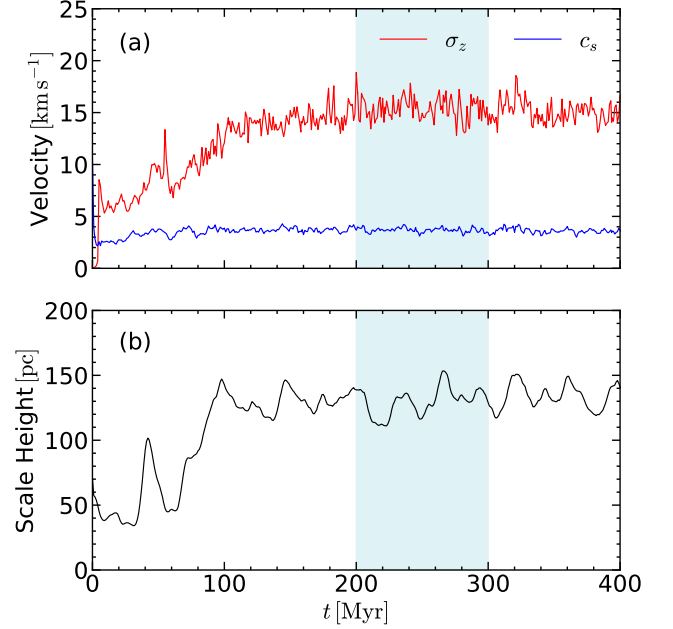


Figure 12. Temporal variations of (a) the vertical velocity dispersion (σ_z ; red) and the sound speed (c_s ; blue) and (b) the scale height H of the cold-warm medium in model L2. The shade indicates the time interval (200–300 Myr) over which time-averaged quantities are evaluated.

$$c_s = \left(\frac{\iint_{z=-\Delta z}^{z=\Delta z} P \Theta \, dx dy dz}{\iint_{z=-\Delta z}^{z=\Delta z} \rho \Theta \, dx dy dz} \right)^{1/2}, \quad (17)$$

$$H = \left(\frac{\iint_{z=-L/2}^{z=L/2} \rho z^2 \Theta \, dx dy dz}{\iint_{z=-L/2}^{z=L/2} \rho \Theta \, dx dy dz} \right)^{1/2}, \quad (18)$$

where $\Delta z = \Delta x$ is the grid spacing along the z -direction and the symbol Θ denotes the phase selector, such that $\Theta = 1$ for the cold-warm medium ($T < 2 \times 10^4$ K) and $\Theta = 0$ otherwise.

Figure 12 plots the temporal history of σ_z , c_s , and H for model L2, showing that these quantities remain more or less constant after $t = 100$ Myr. Note that $\sigma_z \sim 4c_s$ in model L2, indicating that the motions of the cold-warm gas are predominantly supersonic. Table 2 lists the mean values (with standard deviations) of σ_z , c_s , and H averaged over a time span of $\Delta t = 100$ Myr after the system reaches a quasi-steady state.⁴

4. CORRELATIONS OF STATISTICAL QUANTITIES

⁴ We take an average over $t = 300 - 400$ Myr for models L0 and L1 and over $t = 200 - 300$ Myr for all the other models, as the former takes a longer time to reach a steady state.

Table 2. Steady-state properties of the cold-warm gas

Model	σ_z	c_s	H
(1)	(2)	(3)	(4)
	(km s^{-1})	(km s^{-1})	(pc)
L0	8.85 ± 0.66	3.81 ± 0.20	63.88 ± 4.87
L1	12.6 ± 1.0	3.83 ± 0.20	95.0 ± 5.7
L2	15.4 ± 1.1	3.69 ± 0.22	130 ± 11
L3	17.4 ± 1.6	3.30 ± 0.24	151 ± 8
S0	11.9 ± 1.3	3.66 ± 0.31	33.8 ± 1.9
S1	13.1 ± 1.3	3.31 ± 0.32	42.8 ± 2.9
S2	14.8 ± 1.6	2.89 ± 0.28	42.5 ± 2.8
S3	23.6 ± 3.9	2.89 ± 0.35	21.5 ± 2.9

NOTE—(1) Model name. (2) Vertical turbulent velocity dispersion at the midplane. (3) Isothermal sound speed at the midplane. (4) Scale height of the gas.

In this section, we present our measurements of various physical properties of the rings after quasi-steady state is reached, and explore correlations among these properties.

4.1. Ring Properties

To properly characterize the average gas surface density Σ_{ring} of the ring, it is essential to measure the ring area A_{ring} . For this purpose, we place a circular aperture with radius R_c to exclude the gas streams, and take a temporal average ($\langle \Sigma \rangle$) of the gas surface density inside the aperture over a time span of $\Delta t = 100$ Myr after the system reaches a quasi-steady state. We then identify the collection of cells with $\langle \Sigma \rangle > \Sigma_{\text{crit}}$ as the ring region (or ring mask), where Σ_{crit} is determined such that the ring region contains 90% of the total gas mass within R_c . We adjust R_c until it matches the outer semi-major axis of the ring. Figure 13(a) plots as black contours the ring boundaries constructed by this method, overlaid over the time-averaged surface density for model L2. We measure the ring area A_{ring} bounded by the contours, and apply the time-averaged mask to individual snapshots to calculate the ring surface density and the SFR surface density as

$$\Sigma_{\text{ring}} \equiv \frac{M_{\text{ring}}}{A_{\text{ring}}}, \quad (19)$$

$$\Sigma_{\text{SFR}} \equiv \frac{\dot{M}_{\text{SF}}(t, \Delta t = 10 \text{ Myr})}{A_{\text{ring}}}, \quad (20)$$

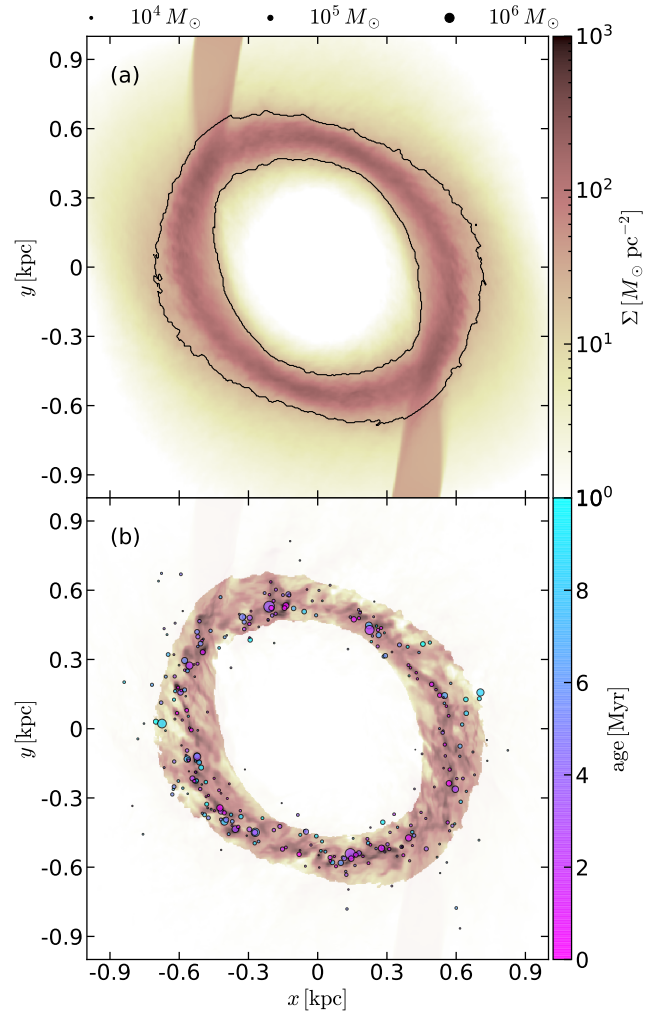


Figure 13. (a) Time-averaged surface density map of model L2. The solid lines delineate the boundaries of the *ring regions*. (b) Example of applying the ring mask to a snapshot of model L2 at $t = 250$ Myr. Quantities such as Σ , Σ_{SFR} , σ , H , etc. are measured inside the ring regions.

where M_{ring} is the gas mass contained in the ring regions. Note that in Equation (20), \dot{M}_{SF} counts sink particles not only inside the ring but also outside the ring since they all have formed inside the ring. The gas depletion time inside the ring is then given by $t_{\text{dep,ring}} = \Sigma_{\text{ring}}/\Sigma_{\text{SFR}}$, which is not much different from t_{dep} over the whole domain defined in Section 3.2 since most mass is contained in the ring. Figure 13(b) overlays the ring mask on top of a surface density map at $t = 250$ Myr for model L2, illustrating that most mass is enclosed within the mask. Table 3 lists the above steady-state physical properties of the rings for all models.

Figure 14 plots the dependence of \dot{M}_{SF} and M_{ring} on \dot{M}_{in} , showing strong correlations. The ring mass

Table 3. Steady-state ring properties

Model	M_{ring}	\dot{M}_{SF}	A_{ring}	Σ_{ring}	Σ_{SFR}	$t_{\text{dep,ring}}$	P_{th}	P_{turb}
(1)	(2)	(3)	(4)	(5)	(6)	(7)	(8)	(9)
	($10^7 M_{\odot}$)	($M_{\odot} \text{ yr}^{-1}$)	(kpc^2)	($M_{\odot} \text{ pc}^{-2}$)	($M_{\odot} \text{ yr}^{-1} \text{ kpc}^{-2}$)	(Myr)	($10^6 k_{\text{B}} \text{ K cm}^{-3}$)	($10^6 k_{\text{B}} \text{ K cm}^{-3}$)
L0	1.25 ± 0.05	0.0897 ± 0.0166	0.607	20.7 ± 0.8	0.148 ± 0.027	144 ± 24	0.128 ± 0.022	0.137 ± 0.022
L1	2.89 ± 0.07	0.425 ± 0.065	0.656	44.0 ± 1.0	0.648 ± 0.099	69.3 ± 9.5	0.424 ± 0.051	0.512 ± 0.079
L2	6.58 ± 0.32	1.67 ± 0.29	0.805	81.8 ± 3.9	2.07 ± 0.37	40.6 ± 7.0	0.966 ± 0.106	1.49 ± 0.19
L3	14.4 ± 0.4	6.98 ± 0.76	0.879	164 ± 5	7.94 ± 0.86	20.9 ± 2.6	1.99 ± 0.32	4.49 ± 0.78
S0	0.263 ± 0.009	0.0891 ± 0.0115	0.0475	55.3 ± 1.8	1.88 ± 0.24	30.0 ± 4.6	1.01 ± 0.30	1.44 ± 0.33
S1	0.619 ± 0.043	0.378 ± 0.056	0.0567	109 ± 8	6.67 ± 0.98	16.8 ± 3.4	2.32 ± 0.42	4.26 ± 0.82
S2	1.43 ± 0.07	1.64 ± 0.15	0.0604	236 ± 12	27.1 ± 2.5	8.81 ± 1.07	3.82 ± 0.78	12.7 ± 2.7
S3	3.66 ± 0.26	6.68 ± 0.52	0.0705	518 ± 37	94.8 ± 7.4	5.52 ± 0.67	9.51 ± 2.06	57.4 ± 19.7

NOTE—(1) Model name. (2) Total gas mass inside the ring. (3) Total star formation rate. (4) Area of the ring. (5) Mean surface density of the ring. (6) Averaged SFR surface density of the ring. (7) Gas depletion time of the ring. (8) Midplane thermal pressure. (9) Midplane turbulent pressure.

in the L series follows a relation $M_{\text{ring}} \approx 4 \times 10^7 M_{\odot} (\dot{M}_{\text{in}}/1 M_{\odot} \text{ yr}^{-1})^{0.6}$, scaled up by a factor ~ 4 relative to the analogous relation for the S series, $M_{\text{ring}} \approx 1 \times 10^7 M_{\odot} (\dot{M}_{\text{in}}/1 M_{\odot} \text{ yr}^{-1})^{0.6}$. In contrast, the SFR is practically the same, $\dot{M}_{\text{SF}} \approx 0.8 \dot{M}_{\text{in}}$, for both series. This demonstrates that in our models the SFR is determined by the mass inflow rate rather than the ring mass. We note that in a given series, M_{ring} varies by a factor of ~ 10 , while \dot{M}_{in} and \dot{M}_{SF} vary by a factor of ~ 80 . This is because Σ_{SFR} is superlinearly proportional to Σ_{ring} , which we will explore in Section 4.2. This appears consistent with observations that ring masses do not vary much among galaxies, while SFRs vary widely (Sheth et al. 2005; Mazzuca et al. 2008).

Figure 15 plots the quasi-steady values of σ_z and H , measured via Equations (16) and (18), against Σ_{SFR} for all models, with errorbars corresponding to the standard deviations. Note that the turbulent velocity dispersion increases weakly with Σ_{SFR} ; the same increasing trend was also seen by Shetty & Ostriker (2012, but for a much smaller range of Σ_{SFR}) and Orr et al. (2020). At low Σ_{SFR} , σ_z is comparable to the solar neighborhood TIGRESS model of Kim & Ostriker (2017). In analogous local-box TIGRESS models with higher gas and stellar density that yield $\Sigma_{\text{SFR}} \sim 0.1 - 1 M_{\odot} \text{ yr}^{-1} \text{ kpc}^{-2}$ (Kim et al. 2020a and Ostriker & Kim 2021, in preparation), the values of σ_z are slightly higher, similar to the results shown here.

The scale height in the S series is smaller than in the L series because of the stronger external gravitational potential. In the L series, H increases with Σ_{SFR} due to the increase in σ_z , while it in the S series is almost

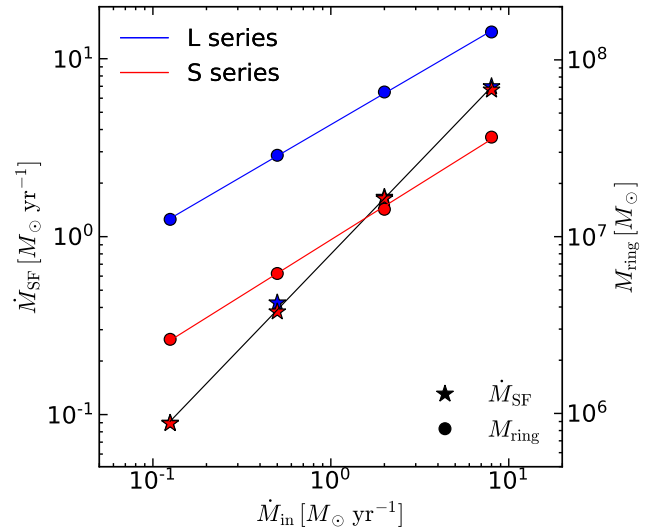


Figure 14. Star formation rate \dot{M}_{SF} (star symbols, left scale) and the ring mass M_{ring} (circles, right scale) against the inflow rate \dot{M}_{in} for all models. The blue and red color correspond to the L and S series, respectively. The solid lines show the linear fits described in the text.

constant or decreases with Σ_{SFR} because of the increased gravity (see below).

4.2. Vertical Dynamical Equilibrium and Star Formation Feedback

Because the nuclear rings in our simulations are not transient but persist over many orbital times, the weight of the ISM, \mathcal{W} , must be supported by the midplane pressure P_{mid} (e.g. Boulares & Cox 1990; Elmegreen & Paravano 1994; Wolfire et al. 2003). The pressure needed

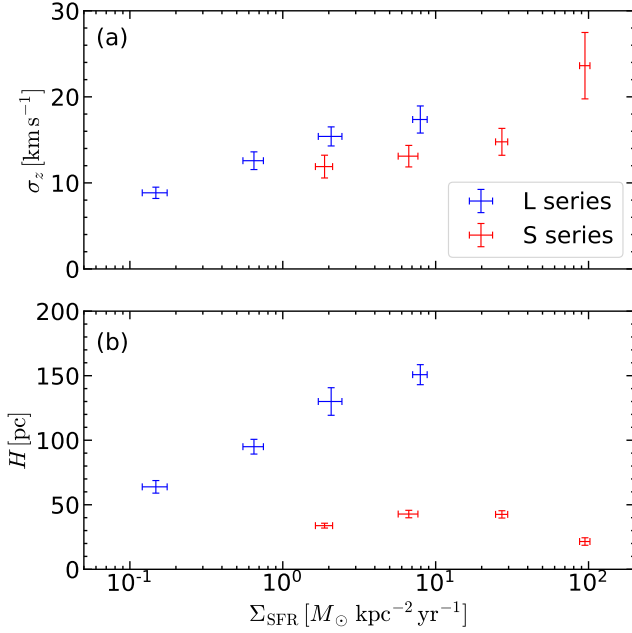


Figure 15. Dependence on the SFR surface density Σ_{SFR} of (a) the time-averaged vertical turbulent velocity dispersion σ_z and (b) the time-averaged vertical scale height H .

for vertical dynamical equilibrium can be maintained only if there are sources of energy and momentum, primarily from young, massive stars (Ostriker et al. 2010; Ostriker & Shetty 2011): the thermal and turbulent pressures would otherwise decay due to radiative cooling and turbulent dissipation on short timescales. In our simulations, the thermal and turbulent pressures are replenished by FUV and CR heating and SN feedback, with the latter being dominant.

4.2.1. Vertical dynamical equilibrium

We measure the midplane thermal and turbulent pressures inside the ring by

$$P_{\text{th}} \equiv \frac{1}{2\Delta z A_{\text{ring}}} \int_{-\Delta z}^{\Delta z} \iint_{A_{\text{ring}}} P \, dx dy dz, \quad (21)$$

$$P_{\text{turb}} \equiv \frac{1}{2\Delta z A_{\text{ring}}} \int_{-\Delta z}^{\Delta z} \iint_{A_{\text{ring}}} \rho v_z^2 \, dx dy dz. \quad (22)$$

We separately measure the weight of the gas due to its own gravitational field, to the gravity of the sink particles, and to the external gravity from the stellar bulge as

$$\mathcal{W}_{\text{gas}} \equiv \frac{1}{A_{\text{ring}}} \iint_{A_{\text{ring}}} \left(\int_0^\infty \rho \frac{\partial \Phi_{\text{gas}}}{\partial z} dz \right) dx dy, \quad (23)$$

$$\mathcal{W}_{\text{sp}} \equiv \frac{1}{A_{\text{ring}}} \iint_{A_{\text{ring}}} \left(\int_0^\infty \rho \frac{\partial \Phi_{\text{sp}}}{\partial z} dz \right) dx dy, \quad (24)$$

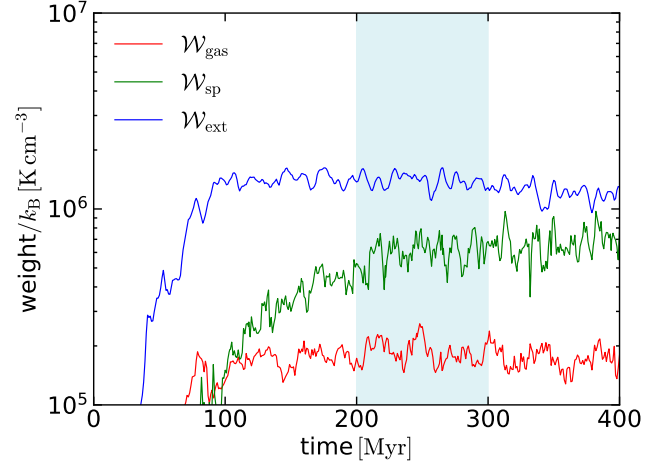


Figure 16. Time evolution of the gas weight contributions due to the gaseous self-gravity (\mathcal{W}_{gas}), the gravity of the sink particles (\mathcal{W}_{sp}), and the external potential (\mathcal{W}_{ext}) in model L2. The shaded region indicates that time span over which the weights are averaged.

$$\mathcal{W}_{\text{ext}} \equiv \frac{1}{A_{\text{ring}}} \iint_{A_{\text{ring}}} \left(\int_0^\infty \rho \frac{\partial \Phi_{\text{ext}}}{\partial z} dz \right) dx dy, \quad (25)$$

where Φ_{gas} and Φ_{sp} refer to the gravitational potential of the gas and sink particles, respectively, such that $\Phi_{\text{self}} = \Phi_{\text{gas}} + \Phi_{\text{sp}}$. Figure 16 plots the temporal evolution of \mathcal{W}_{gas} , \mathcal{W}_{sp} , and \mathcal{W}_{ext} of model L2 as red, green, and blue lines, respectively. After the system reaches a quasi-steady state ($t \gtrsim 100$ Myr), \mathcal{W}_{ext} and \mathcal{W}_{gas} do not vary much, while \mathcal{W}_{sp} keeps increasing due to the continuous creation of the sink particles. The time-averaged weights over $t = 200 - 300$ Myr are $\mathcal{W}_{\text{gas}}/k_B = 1.9 \times 10^5 \text{ K cm}^{-3}$, $\mathcal{W}_{\text{sp}}/k_B = 6 \times 10^5 \text{ K cm}^{-3}$, and $\mathcal{W}_{\text{ext}}/k_B = 1.4 \times 10^6 \text{ K cm}^{-3}$, indicating that the gas weight in model L2 is mostly due to Φ_{sp} and Φ_{ext} rather than Φ_{gas} .

We now compare the total midplane pressure $P_{\text{mid}} = P_{\text{th}} + P_{\text{turb}}$ with the total weight $\mathcal{W}_{\text{tot}} = \mathcal{W}_{\text{gas}} + \mathcal{W}_{\text{sp}} + \mathcal{W}_{\text{ext}}$ of the ISM, checking to what extent vertical dynamical equilibrium holds. Vertical dynamical equilibrium requires

$$P_{\text{mid}} - P_{\text{top}} = \mathcal{W}_{\text{tot}}, \quad (26)$$

where P_{top} is the total pressure at the top boundary ($z = L/2$) defined as

$$P_{\text{top}} \equiv \frac{1}{A_{\text{ring}}} \iint_{A_{\text{ring}}} (P + \rho v_z^2)_{z=L/2} dx dy. \quad (27)$$

In normal situations, $P_{\text{top}} \ll P_{\text{mid}}$, leading to the usual equilibrium condition $P_{\text{mid}} \approx \mathcal{W}_{\text{tot}}$. If a system develops

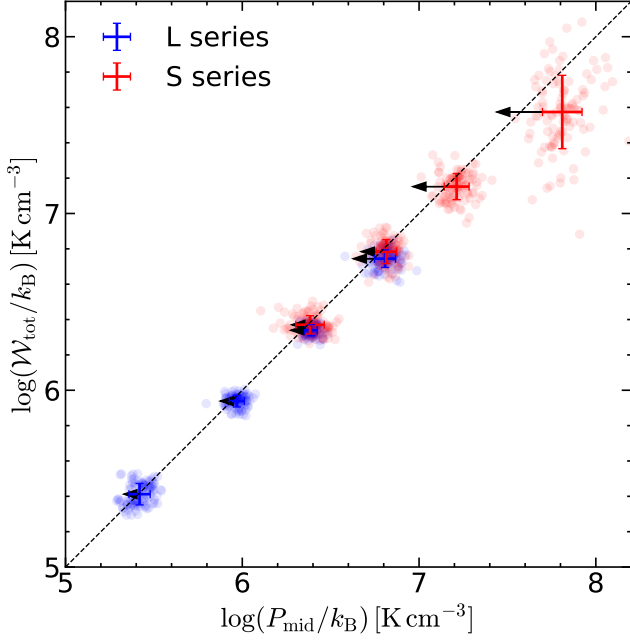


Figure 17. Total weight of the ISM against the total mid-plane pressure. Each circle corresponds to a different snapshot during $t = 200 - 300$ Myr. Errorbars denote the temporal averages and standard deviations of each model. The dashed line corresponds to $\mathcal{W}_{\text{tot}} = P_{\text{mid}}$. Black arrows indicate the shifts of the mean values in the abscissa when P_{mid} is changed to $P_{\text{mid}} - P_{\text{top}}$.

strong outflows with high ram pressure and the vertical extent is small, however, P_{top} may no longer be negligible compared to the midplane pressure.

Figure 17 plots for individual snapshots \mathcal{W}_{tot} against P_{mid} over the interval $\Delta t = 100$ Myr after steady state is reached, using blue and red for the L and S series, respectively. Additionally, points with errorbars indicate means and standard deviations for each model. All models closely follow the $\mathcal{W}_{\text{tot}} = P_{\text{mid}}$ line, except for models S2 and S3 which lie slightly below the line. The black arrows denote the shifts of the mean values in the abscissa when P_{mid} is changed to $P_{\text{mid}} - P_{\text{top}}$, indicating that P_{top} is significant ($\approx 0.4P_{\text{mid}}$) in models S2 and S3. After correcting for P_{top} , all models satisfy Equation (26), demonstrating that vertical dynamical equilibrium is maintained in an averaged sense.

4.2.2. Scaling relations of the gas weights

Figure 18 plots the time-averaged gas weights of all models against Σ_{ring} . For a plane-parallel slab with total gas surface density Σ_{ring} , $\mathcal{W}_{\text{gas}} \approx \pi G \Sigma_{\text{ring}}^2 / 2$; while this does not apply exactly given the ring geometry, a quadratic scaling is still expected. If the scale height of the gas disk is larger than that of young stars but smaller than that of old stars, the corresponding weights for hor-

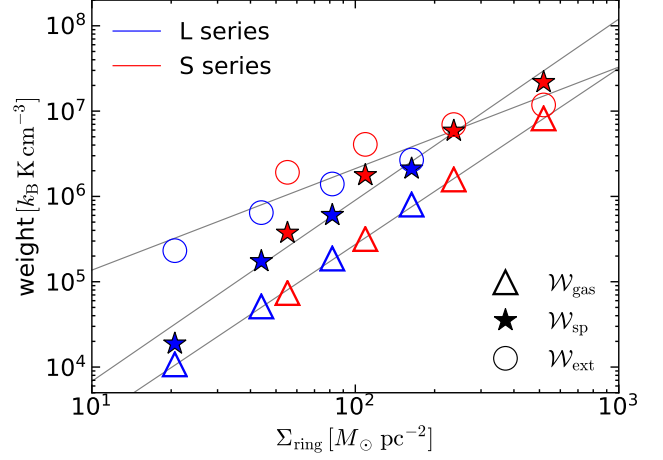


Figure 18. Dependence of the gas weights on the ring surface density. Blue and red symbols correspond to the L and S series, respectively. Triangles, stars, and circles represent the gas weight due to the gaseous self-gravity, the gravity of the sink particles, and the external potential, respectively. All quantities are averaged over $\Delta t = 100$ Myr. Lines are linear fits to the numerical results with slopes of 2.07, 2.12, and 1.19 for \mathcal{W}_{gas} , \mathcal{W}_{sp} , and \mathcal{W}_{ext} , respectively.

izontally uniform disks would be $\mathcal{W}_{\text{sp}} \approx \pi G \Sigma_{\text{ring}} \Sigma_{\text{sp}}$ and $\mathcal{W}_{\text{ext}} \approx \Sigma_{\text{ring}} \sigma_z (2G \rho_b / 3)^{1/2}$, where Σ_{sp} is the surface density of the sink particles, ρ_b is the volume density of old stars in the bulge at the midplane, and a Gaussian vertical profile is assumed (Ostriker & Shetty 2011); again these can only be approximate given the ring geometry, bulge stratification, etc.

Assuming that the weights are proportional to Σ_{ring}^p with a power-law index p , simple linear fits to our results yield $p = 2.07$, 2.12, and 1.19 for \mathcal{W}_{gas} , \mathcal{W}_{sp} , and \mathcal{W}_{ext} , respectively. These are broadly consistent with the above prediction, under the condition that Σ_{sp} is roughly proportional to Σ_{ring} and that σ_z depends on Σ_{ring} only weakly (from Figure 15).⁵ Although the gas disks in our models neither have a plane-parallel geometry nor are well described by a Gaussian vertical profile, deviations of each weight contributions measured using Equations (23)–(25) from analytical predictions are at most a factor of ~ 3 .

The total weight of the gas is dominated by \mathcal{W}_{ext} at low Σ_{ring} , while \mathcal{W}_{sp} also becomes significant at high Σ_{ring} . For all models, self-gravity has a relatively mi-

⁵ Since ρ_b is larger for the S series than the L series, \mathcal{W}_{ext} is offset upward for the former, as expected from $\mathcal{W}_{\text{ext}} \propto \Sigma_{\text{ring}} \sqrt{\rho_b}$. With a constant SFR, $\Sigma_{\text{sp}} \propto \Sigma_{\text{SFR}} t$. We shall show that from self-regulation, Σ_{SFR} varies approximately linearly in \mathcal{W}_{tot} , so for weight dominated by the external potential we expect $\Sigma_{\text{sp}} \propto \Sigma_{\text{ring}} t \sigma_z \sqrt{\rho_b}$, which would then yield $\mathcal{W}_{\text{sp}} \propto \Sigma_{\text{ring}}^2 t \sigma_z \sqrt{\rho_b}$.

nor contribution to the total weight, different from the models of Ostriker & Shetty (2011) and Shetty & Ostriker (2012). There, the weight in the external potential was (by design) smaller than the weight of the gas, and the weight from star particles was not considered because it was implicitly assumed that the starburst had a sufficiently short duration that significant stellar mass did not build up (the present models show that this indeed requires hundreds of Myr). In the local simulations of Ostriker & Shetty (2011) and Shetty & Ostriker (2012), M_{gas} did not build up over time but was imposed from the initial conditions, so it could be large without also having M_{sp} large (unlike the case for the present models, per Figure 14). In the present simulations, the value of ρ_b in the ring region is relatively large, because nuclear rings form more easily in the presence of a strong central concentration (Athanasoula 1992; Regan & Teuben 2003; Li et al. 2015). We note that if the star formation efficiency within the sink particles is not 100%, only a fraction of W_{sp} would be regarded as being self-gravitational. In creating a sink particle, we assume that all of the gas in a cell is immediately converted to a star cluster. In contrast, Tress et al. (2020) assumed only 5% of the sink particle mass actually represents the mass of the star cluster, while treating the remaining 95% as gas ‘temporarily stored’ in the sink particles which is later returned to the ambient ISM via SN feedback. We have adopted the current approach for simplicity, but in future work it would be quite interesting to test whether a treatment of sink particles with mass loss would change the results for the various scaling relations studied in this work.

4.2.3. Pressure scaling relations and the feedback yields

As expected, the pressures are directly correlated with the star formation rate per unit area. Figure 19 plots P_{th} and P_{turb} against Σ_{SFR} as points with errorbars, corresponding to the mean values and standard deviations, respectively. Our best fits, including both the S and L series, are

$$\frac{P_{\text{th}}}{k_B} = 5.47 \times 10^5 \text{ cm}^{-3} \text{ K} \left(\frac{\Sigma_{\text{SFR}}}{M_{\odot} \text{ kpc}^{-2} \text{ yr}^{-1}} \right)^{0.64}, \quad (28)$$

$$\frac{P_{\text{turb}}}{k_B} = 7.56 \times 10^5 \text{ cm}^{-3} \text{ K} \left(\frac{\Sigma_{\text{SFR}}}{M_{\odot} \text{ kpc}^{-2} \text{ yr}^{-1}} \right)^{0.89}, \quad (29)$$

plotted as solid lines. The thermal pressure increases with Σ_{SFR} sublinearly because of the adopted FUV shielding that is stronger for models with higher \dot{M}_{in} . The turbulent pressure driven by SN feedback is proportional almost linearly to Σ_{SFR} . As a result, the

turbulent pressure dominates the thermal pressure for high Σ_{SFR} models, consistent with Ostriker & Shetty (2011). Figure 19 also shows, for comparison, results from simulations in Shetty & Ostriker (2012) modeling starburst regions, and the extrapolation of the relation $P_{\text{turb}}/k_B = 2.0 \times 10^6 \text{ cm}^{-3} \text{ K} (\Sigma_{\text{SFR}}/M_{\odot} \text{ kpc}^{-2} \text{ yr}^{-1})^{0.89}$ found by Kim et al. (2013) (see their Equation 21) based on local simulations of normal star-forming galactic environments.

Equations (28) and (29) can be rewritten as

$$P_{\text{th}} = \Upsilon_{\text{th}} \Sigma_{\text{SFR}}, \quad (30)$$

$$P_{\text{turb}} = \Upsilon_{\text{turb}} \Sigma_{\text{SFR}}. \quad (31)$$

where Υ_{th} and Υ_{turb} are the thermal⁶ and the turbulent feedback yields, respectively, given by

$$\Upsilon_{\text{th}} = 114 \text{ km s}^{-1} \left(\frac{\Sigma_{\text{SFR}}}{M_{\odot} \text{ kpc}^{-2} \text{ yr}^{-1}} \right)^{-0.36}, \quad (32)$$

$$\Upsilon_{\text{turb}} = 158 \text{ km s}^{-1} \left(\frac{\Sigma_{\text{SFR}}}{M_{\odot} \text{ kpc}^{-2} \text{ yr}^{-1}} \right)^{-0.11}. \quad (33)$$

The feedback ‘yield’ for individual pressure terms was introduced by Kim et al. (2011a) (see their Equations 11 and 12). There, and also in Kim et al. (2013) and Kim & Ostriker (2015a), the notation η was adopted for the ratio between P and Σ_{SFR} , adopting common astronomical units of $10^3 k_B \text{ cm}^{-3} \text{ K}$ for the former and $10^{-3} M_{\odot} \text{ kpc}^{-2} \text{ yr}^{-1}$ for the latter so that η is dimensionless. Since the ratio between P and Σ_{SFR} is a naturally a velocity, we instead adopt units of km s^{-1} for yields Υ . The conversion is $\Upsilon/\text{km s}^{-1} = 209\eta$. The turbulent yield in the present work is a factor $\sim 2 - 3$ smaller than that of Shetty & Ostriker (2012) and the extrapolation of Kim et al. (2013), where the latter is $\Upsilon_{\text{turb}} = 420 \text{ km s}^{-1} (\Sigma_{\text{SFR}}/M_{\odot} \text{ kpc}^{-2} \text{ yr}^{-1})^{-0.1}$ (converting from their Equation 23 to the present units). For the set of TIGRESS simulations described in Kim et al. (2020a), analysis to be presented in Ostriker & Kim (2021, in prep.) also finds $\Upsilon_{\text{turb}} \propto \Sigma_{\text{SFR}}^{-0.1}$, with a coefficient $\sim 70\%$ higher than in Equation (33). In Section 5.2, we will discuss possible causes for the lower Υ_{turb} in the present models and star-forming rings more generally.

4.2.4. Scaling relations of the star formation rate

It is of much interest to determine what large-scale galactic properties provide the best prediction for the star formation rate. A simple correlation that has been

⁶ In our simulations, the thermal pressure mostly comes from hot bubbles created by SN feedback rather than FUV heating.

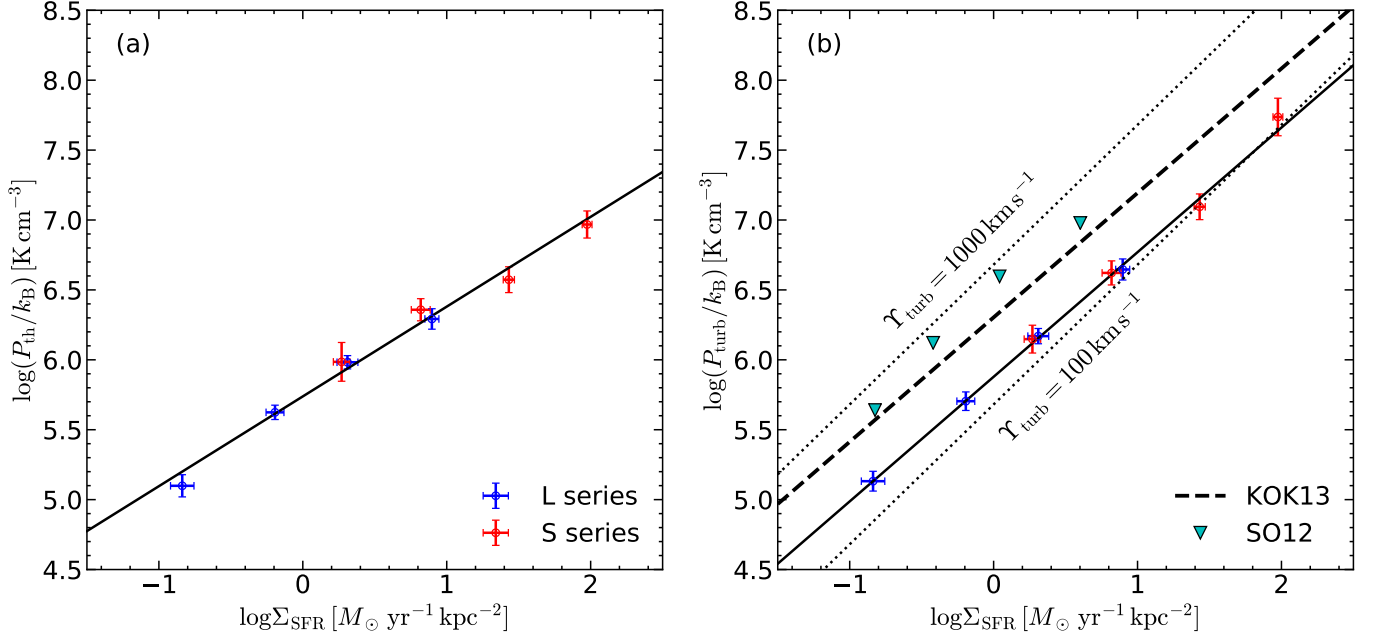


Figure 19. Mean (a) thermal and (b) turbulent pressure at the midplane, plotted against the mean SFR surface density within the ring, for each model (see also Table 3). The solid lines are the linear fits, Equations (28) and (29). In (b), cyan triangles are the results of Shetty & Ostriker (2012, Series S), while the dashed line is the extrapolation of Equation (21) from Kim et al. (2013). The two dotted lines correspond to $\Upsilon_{\text{turb}} = 100 \text{ km s}^{-1}$ and 1000 km s^{-1} for reference.

extensively investigated empirically is the Kennicutt-Schmidt relation between gas and star formation surface densities (Schmidt 1959; Kennicutt 1998). Figure 20(a) plots Σ_{SFR} against Σ_{ring} for all of our models. A linear fit to our models yields

$$\Sigma_{\text{SFR}} = 3.0 M_{\odot} \text{ yr}^{-1} \text{ kpc}^{-2} \left(\frac{\Sigma_{\text{ring}}}{10^2 M_{\odot} \text{ pc}^{-2}} \right)^{1.9}, \text{ for L series,} \quad (34a)$$

$$\Sigma_{\text{SFR}} = 5.5 M_{\odot} \text{ yr}^{-1} \text{ kpc}^{-2} \left(\frac{\Sigma_{\text{ring}}}{10^2 M_{\odot} \text{ pc}^{-2}} \right)^{1.8}, \text{ for S series.} \quad (34b)$$

While these have similar scalings with Σ_{ring} , the distinct offset between the relations for the two series makes plain that an additional parameter contributes in regulating Σ_{SFR} : surface density is not by itself sufficient.

In the theory of feedback-modulated, self-regulated star formation, the key large-scale parameter is not the gas surface density by itself, but the combination of gas and stellar parameters that go into defining the ISM weight \mathcal{W} , as described above. The individual components of pressure scale as power laws in Σ_{SFR} (the source of heat and turbulence), as shown in Figure 19, and the pressure balances the gas weight, as shown in Figure 17. Since turbulence dominates the pressure in galactic center environments and Υ_{turb} varies only weakly, we expect a nearly linear scaling of Σ_{SFR} with P_{mid} or \mathcal{W} , and this is indeed evident in Figure 20(b),(c).

Quantitatively we find that both the L and S series follow a single relation

$$\Sigma_{\text{SFR}} = 0.71 M_{\odot} \text{ yr}^{-1} \text{ kpc}^{-2} \left(\frac{P_{\text{mid}}/k_B}{10^6 \text{ cm}^{-3} \text{ K}} \right)^{1.2}, \quad (35)$$

or

$$\Sigma_{\text{SFR}} = 0.75 M_{\odot} \text{ yr}^{-1} \text{ kpc}^{-2} \left(\frac{\mathcal{W}_{\text{tot}}/k_B}{10^6 \text{ cm}^{-3} \text{ K}} \right)^{1.3}, \quad (36)$$

which are plotted as dashed lines in Figure 20(b),(c). For comparison, the extrapolation of Equation (26) from Kim et al. (2013) is $\Sigma_{\text{SFR}} = 0.48 M_{\odot} \text{ yr}^{-1} \text{ kpc}^{-2} (P_{\text{mid}}/10^6 \text{ cm}^{-3} k_B \text{ K})^{1.18}$, lower by a factor ~ 1.5 . Similarly, the extrapolation of Equation (27) from Kim et al. (2013) is $\Sigma_{\text{SFR}} = 0.33 M_{\odot} \text{ yr}^{-1} \text{ kpc}^{-2} (\mathcal{W}_{\text{tot}}/10^6 \text{ cm}^{-3} k_B \text{ K})^{1.13}$, lower by a factor ~ 2.3 . In local-disk TIGRESS simulations, the coefficients in the relations corresponding to Equations (35)-(36) are lower by factors 2.5 – 3 (Ostriker & Kim 2021, in prep.). We discuss in Section 5.2 possible reasons for these offsets in Σ_{SFR} -pressure relations. The better agreement between S and L series in (b) and (c) than in (a) suggest that the $\Sigma_{\text{SFR}}-P_{\text{mid}}$ (or $\Sigma_{\text{SFR}}-\mathcal{W}_{\text{tot}}$) relation is more fundamental than the $\Sigma_{\text{SFR}}-\Sigma_{\text{ring}}$ relation for regulation of star formation in nuclear rings.

We can use the Σ_{SFR} -pressure relation together with our previous results for scalings to interpret dependences of Σ_{SFR} on Σ_{ring} . At given Σ_{ring} , the S series shows enhanced Σ_{SFR} compared to the L series because of the

stronger external gravity, which increases \mathcal{W}_{tot} . This in turn requires higher Σ_{SFR} to maintain a higher P_{mid} through feedback. However, the enhancement of Σ_{SFR} is only a factor of ~ 2 , despite a factor of 11 difference in $\rho_b(R_{\text{ring}})$. This is because stronger gravity and slightly lower σ_z makes the disk thinner in the S series (with $H \propto \sigma_z/\sqrt{\rho_b}$), leading to only a modest increase in the weight $\mathcal{W}_{\text{ext}} \propto \rho_b H \propto \sqrt{\rho_b} \sigma_z$ of the ISM for given surface density. The difference in the external stellar potential is the main reason that the $\Sigma_{\text{SFR}}-\Sigma_{\text{ring}}$ relation is different between the L and S series.

As noted above, the three weight contributions are roughly given by $\mathcal{W}_{\text{gas}} \sim \pi G \Sigma_{\text{ring}}^2/2$, $\mathcal{W}_{\text{sp}} \sim \pi G \Sigma_{\text{ring}} \Sigma_{\text{sp}}$, and $\mathcal{W}_{\text{ext}} \sim \Sigma_{\text{ring}} \sigma_z (2G\rho_b/3)^{1/2}$. Although \mathcal{W}_{ext} is the largest among the three (except for the S3 model), the contribution from \mathcal{W}_{sp} becomes quite significant as Σ_{ring} increases. Because of this (and since Σ_{sp} increases with Σ_{ring}), the total weight increases super-linearly with surface density (a fit gives $\mathcal{W}_{\text{tot}} \sim \Sigma_{\text{ring}}^{1.54}$). Meanwhile, Equation (35) indicate the total feedback yield $\Upsilon_{\text{tot}} \equiv P_{\text{mid}}/\Sigma_{\text{SFR}}$ decreases with Σ_{SFR} as $\Upsilon_{\text{tot}} = 277 \text{ km s}^{-1} (\Sigma_{\text{SFR}}/M_{\odot} \text{ yr}^{-1} \text{ kpc}^{-2})^{-0.17}$. These two effects act together to steepen the $\Sigma_{\text{SFR}} - \Sigma_{\text{ring}}$ relation via $\Sigma_{\text{SFR}} \propto \Upsilon_{\text{tot}}^{-1} \mathcal{W}_{\text{tot}} \propto \Sigma_{\text{ring}}^{1.86}$. Although the weight in our simulations is dominated by \mathcal{W}_{ext} and \mathcal{W}_{sp} rather than \mathcal{W}_{gas} , it happens that the dependence of Σ_{sp} on Σ_{ring} makes the $\Sigma_{\text{SFR}}-\Sigma_{\text{ring}}$ relation close to the self-gravity dominated case, as in [Ostriker & Shetty \(2011\)](#) and [Shetty & Ostriker \(2012\)](#).

5. SUMMARY AND DISCUSSION

5.1. Summary

Nuclear rings are the sites of compact and extremely vigorous star formation, powered by bar-driven inflows from the larger-scale ISM. Despite many observational and theoretical studies of nuclear rings, it has remained unclear what determines the gas ring’s properties and SFR, and how star formation in nuclear rings proceeds with time. To address these issues, we construct a semi-global model of a nuclear ring where the bar-driven mass inflows are treated by the boundary conditions. An advantage of our framework over fully global simulations is that it enables us to directly control the mass inflow rate and ring radius.

We have modified the TIGRESS framework ([Kim & Ostriker 2017](#)) for self-consistently simulating the star-forming ISM to make it suitable for galactic center regions with non-periodic boundary conditions. As before, gravitational collapse leading to star formation and feedback utilizes sink particles that model star clusters, which produce FUV heating and SN explosions. To account for the shielding of FUV radiation in high density

environments expected in nuclear rings, we make the FUV intensity decrease exponentially with local density (Equation 10). To balance cooling in these heavily shielded region, we include a simplified treatment of CR heating by ionization (Equation 11).

We have run two series of models that differ in the specific angular momentum of the inflow and therefore the resulting ring size R_{ring} : models in the S series have small rings with $R_{\text{ring}} = 150 \text{ pc}$ and models in the L series have large rings with $R_{\text{ring}} = 600 \text{ pc}$. While the gravitational potential profile is the same for the two series, the ring gas in the S series experiences stronger vertical compression than the L series because the vertical gravity is stronger closer to the galactic center. The initial gas distribution is near-vacuum and the subsequent evolution is governed by the gas inflows through two nozzles located at the y -boundaries (Figure 3). In each series, we consider four models that differ in the mass inflow rate \dot{M}_{in} (Table 1). We run all models beyond $t = 300 \text{ Myr}$, long enough for the system to reach a quasi-steady state.

The main results of the present work can be summarized as follows:

1. *Overall Evolution* — Inflowing gas streams collide with each other after half an orbit, forming strong shocks at the contact points between the streams. As the orbital kinetic energy is lost, the gas streams gradually circularize to make a nuclear ring. Star formation soon becomes widely distributed along the whole length of the ring, and SN feedback produces hot gas that fills most of the volume. Within $\sim 100 \text{ Myr}$, the system reaches a quasi-steady state in which the gas properties and the SFR do not vary much with time.
2. *Star Formation and Feedback* — In the quasi-steady state, star formation occurs throughout the ring and the SFR exhibits only modest (within a factor of ~ 2) temporal fluctuations. For both the L and S series, the SFR is solely determined by the inflow rate as $\dot{M}_{\text{SF}} \approx 0.8 \dot{M}_{\text{in}}$. The ring gas mass $M_{\text{ring}} \propto \dot{M}_{\text{in}}^{0.6}$, with the rings in the S series about four times less massive than in the L series.

SN from clusters create many holes along the ring as superbubbles break out, but the feedback never destroys the entire ring. As the star particles diffuse out of the ring, SN from relatively old clusters can occur outside of the ring, dumping most of their energy in the ambient hot medium rather than the ring gas. Because SN feedback is “wasted” outside of the ring gas, a higher SFR is required to maintain equilibrium than would be

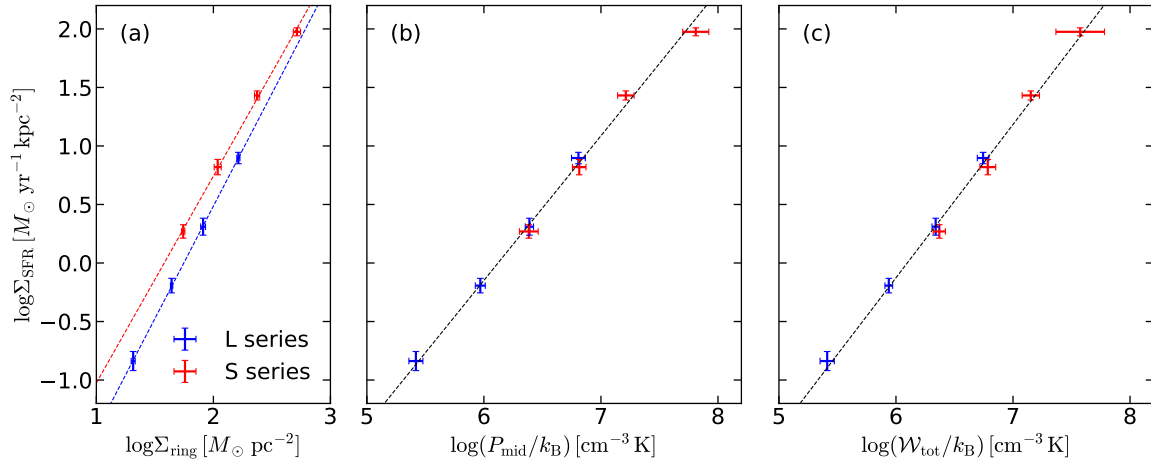


Figure 20. Dependence of the SFR surface density Σ_{SFR} on (a) the ring surface density Σ_{ring} , (b) the midplane pressure P_{mid} , and (c) the total gas weight \mathcal{W}_{tot} . The L and S series lie on different lines, Equation (34), in the $\Sigma_{\text{SFR}}-\Sigma_{\text{ring}}$ plane. In contrast, the two series follow the same relation, Equation (35), over nearly three orders of magnitude in the $\Sigma_{\text{SFR}}-P_{\text{mid}}$ or $\Sigma_{\text{SFR}}-\mathcal{W}_{\text{tot}}$ plane. The pressure (or weight) provides a better predictor for star formation than gas surface density alone because it allows for (varying) compression of the ISM by the stellar potential.

needed if the gas and SNe were cospatial in a more uniform disk.

3. *Winds* — Our models naturally develop biconical, helically outflowing winds due to SN feedback (Figure 8). The opening up of the gas streamlines allows the winds accelerate from subsonic to supersonic velocities, readily reaching $\sim 600\text{--}900 \text{ km s}^{-1}$ at $z = 1 \text{ kpc}$, with the largest velocity occurring near the symmetry axis ($R = 0$).
4. *Ring Properties* — Most of the mass is in cold-warm gas, with pressure and density close to the thermal equilibrium curve in which radiative cooling is balanced by FUV and CR heating. Dissipation of kinetic energy is also a significant heating source for the cold-unstable phase with $T < 5050 \text{ K}$. The mean sound speed of the cold-warm gas is only $\sim 3 - 4 \text{ km s}^{-1}$ (Table 2), much lower than the turbulent velocity dispersion $\sigma_z \sim (10\text{--}25) \text{ km s}^{-1}$, which mildly increases with Σ_{SFR} (Figure 15). The scale height increases monotonically with Σ_{SFR} due to an increase in σ_z in the L series, while it is roughly constant or decreases for high Σ_{SFR} due to the increased gravity of star particles in the S series.

Rings are more eccentric for models with larger \dot{M}_{in} and/or smaller R_{ring} . Gas in these models tends to have shorter t_{dep} , and is thus rapidly depleted by star formation before the orbits can be fully circularized. In eccentric gas rings, the orbits of young star particles also inherit large eccentricities. Due to the precession of orbits, however, the

distribution of old star particles is more or less circular, regardless of the ring shape.

5. *Vertical Dynamical Equilibrium* — The ISM in the nuclear rings satisfies vertical dynamical equilibrium, in which the total pressure (turbulent exceeding thermal) balances the weight of the gas. The pressure at the z -boundaries is non-negligible in models with strong outflows and small vertical extent (Figure 17). For the parameters of our models, the weight is dominated mostly by the external gravity term, with the gravity of the newly created sink particles making a secondary contribution. Because the gas is consumed rapidly, the self-gravity term does not become large. Scalings of \mathcal{W}_{ext} , \mathcal{W}_{sp} , and \mathcal{W}_{gas} with the gas surface density in the ring, Σ_{ring} , are consistent with expectations.
6. *Scaling Relations for Pressure and Star Formation*

Consistent with expectations for driving by momentum injection from SNe, the turbulent pressure varies nearly linearly with the SFR surface density (Equation 29). The corresponding turbulent yield Υ_{turb} (Equation 33) is a factor $\sim 2\text{--}3$ smaller than the values in local-box simulations; this reduced efficiency may be due to feedback that is “lost” when SNe go off outside of the ring.

The combination of vertical dynamical equilibrium with the $P_{\text{turb}}-\Sigma_{\text{SFR}}$ relation leads to a nearly linear dependence of Σ_{SFR} on P_{mid} (or the total weight \mathcal{W}_{tot}), given by Equation (35) (or 36). Both the S and L series lie along a single relation.

The power is the same as found by Kim et al. (2013), while the coefficient is a factor $\sim 1.5 - 2.3$ higher due to the reduced feedback efficiency.

For the individual S and L series, there are power-law relationships between Σ_{SFR} and Σ_{ring} with slopes between 1 and 2, consistent with expectations for scalings intermediate between $\Sigma_{\text{SFR}} \propto \mathcal{W}_{\text{ext}} \propto \Sigma_{\text{ring}}$ and $\Sigma_{\text{SFR}} \propto \mathcal{W}_{\text{sp}} + \mathcal{W}_{\text{gas}} \propto \Sigma_{\text{ring}}^2$. However, the S series is offset to higher Σ_{SFR} than the L series due to the stronger vertical gravity of the bulge at the locations of the smaller rings.

Importantly, we conclude that the $\Sigma_{\text{SFR}} - P_{\text{mid}}$ (or \mathcal{W}_{tot}) relation is more general (as well as more physically fundamental) than the $\Sigma_{\text{SFR}} - \Sigma_{\text{ring}}$ relation. The pressure relation provides a better predictor for star formation because it explicitly allows for variations in the vertical compression of the ISM by stellar gravity, which differ with environment even within a given galactic center region.

5.2. Discussion

Inflows and star formation—Our results show that the ring SFR, \dot{M}_{SF} , is controlled primarily by the mass inflow rate \dot{M}_{in} rather than the ring mass. This is overall consistent with the numerical results that the ring SFR is, when averaged over a few 100 Myrs, roughly equal to the mass inflow rate to the ring in global simulations of barred galaxies (Seo & Kim 2013, 2014; Seo et al. 2019), suggesting that observed star formation histories in nuclear rings (e.g., Allard et al. 2006; Sarzi et al. 2007; Gadotti et al. 2019) may primarily reflect the time variations in the mass inflow rates. The strong correlation between \dot{M}_{SF} and \dot{M}_{in} is a direct (and causal) consequence of the mass conservation: in our models, 80% of the inflowing gas is consumed by star formation, while the remaining 20% is ejected as galactic winds. While \dot{M}_{SF} and M_{ring} , or Σ_{SFR} and Σ_{ring} , are also correlated, this relationship is more indirect, depending on environmental parameters such as the external gravity and on the feedback strength (see Section 4.2). In fact, given that \dot{M}_{SF} appears to be causally determined by \dot{M}_{in} , M_{ring} may be considered as *responding* to the inflow rate. That is, $M_{\text{ring}} \sim t_{\text{dep}} \dot{M}_{\text{in}}$, where in some circumstances the depletion time is relatively insensitive to the ring properties and depends primarily on the bulge potential (see below).

In our semi-global simulations, \dot{M}_{in} is fixed to a constant value and the resulting \dot{M}_{SF} and t_{dep} do not change appreciably with time (see discussion of t_{dep} below). Our simulations do not have the boom/bust behavior of other models (e.g., Kruijssen et al. 2014; Krumholz et al. 2017; Torrey et al. 2017; Armillotta et al. 2019) be-

cause star formation is distributed throughout the ring and the associated feedback is never strong enough to disperse the ring or make it quiescent as a whole. The recent global simulations of Sormani et al. (2020) also found that the depletion time in the CMZ is roughly constant, with the SFR varying linearly with the CMZ mass, which is most likely affected by the mass inflow rate.

Our models employ a steady and symmetric injection of gas streams from two nozzles. The simple, symmetric inflow we impose is intentionally idealized, since this is our first study of nuclear star formation with a new numerical framework. The inflow results in the formation of nuclear rings over which gas and star particles are roughly uniformly distributed. A visual inspection of the nuclear rings in 78 barred galaxies presented by Comerón et al. (2010) shows that rings with symmetric star formation are more common than those with lopsided star formation.⁷ Nevertheless, there are notable examples of lopsided nuclear rings, including our own CMZ (e.g., Barnes et al. 2017; Henshaw et al. 2016) and the ring in M83 (e.g., Harris et al. 2001). Asymmetric star formation in such rings may be caused by the mass inflow rates that are highly asymmetric and nonsteady (e.g., Harada et al. 2019). Large-scale simulations (e.g. Seo et al. 2019; Armillotta et al. 2019; Tress et al. 2020) with time-varying, asymmetric inflows, as well as observations (e.g., Sormani & Barnes 2019) motivate further study of lopsided ring formation at high resolution, and we plan to explore this question in a forthcoming paper.

Feedback yield—The turbulent yield (Equation 33) in our simulations is smaller than the value in the previous simulations with SN feedback of Shetty & Ostriker (2012) and Kim et al. (2013). Considering the balance between the turbulent driving and dissipation, Ostriker & Shetty (2011) showed that the turbulent yield is given by $\Upsilon_{\text{turb}} = f_p p_* / (4m_*)$, where p_* is the asymptotic radial momentum injected per SN and m_* is the total mass in stars per SN ($m_* \approx 100 M_\odot$ for a Kroupa IMF). The parameter f_p encapsulates details of the driving and dissipation and is expected to be $f_p \sim 0.5 - 2$, with tests showing $f_p \approx 1$ for a range of parameters, and a slight decreasing trend towards higher SFR (Ostriker & Shetty 2011; Shetty & Ostriker 2012; Kim et al. 2011a, 2013). Kim et al. (2013) and Kim & Ostriker (2015a) (including magnetic fields) adopted $p_* = 3 \times 10^5 M_\odot \text{ km s}^{-1}$ as a fiducial value (based on isolated SNe in uniform gas), and found $\Upsilon_{\text{turb}} \sim 700 - 900 \text{ km s}^{-1}$ for solar-

⁷ Color composite images of 16 symmetric rings among the sample are available in Ma et al. (2018).

neighborhood conditions (irrespective of magnetic field strengths; see Kim & Ostriker 2015a), decreasing to $\Upsilon_{\text{turb}} \sim 500 \text{ km s}^{-1}$ for a factor ~ 20 higher SFR. In a local-disk TIGRESS suite (Kim et al. 2020a, Ostriker & Kim 2021 in prep.), exploring more extreme conditions up to $\Sigma_{\text{SFR}} \sim 1 M_{\odot} \text{ yr}^{-1} \text{ kpc}^{-2}$, Υ_{turb} further decreases to $\sim 270 \text{ km s}^{-1}$, which is about $\sim 36\%$ lower than an extrapolation from Kim et al. (2013) and 70% larger than what we found in this paper (Equation 33).

It should be noted that $\sim 80\text{--}90\%$ of all SNe in our simulations are resolved so that, as in the local-disk TIGRESS suite, p_* is determined self-consistently via non-linear gas interactions. Assuming $f_p = 1$, Equation (33) translates to $p_* \sim 0.4 - 0.8 \times 10^5 M_{\odot} \text{ km s}^{-1}$. This is a factor of ~ 5 lower than what was found for isolated SNe at densities comparable to solar neighborhood ISM, but closer to the momentum injection in high density environments (e.g. Kim & Ostriker 2015b; Martizzi et al. 2015), and also quite comparable to results from experiments in which multiple SNe explode at short (~ 0.01 Myr) intervals for a range of ambient density (Kim et al. 2017a). This could explain the generally smaller turbulent feedback yield in simulations using the full TIGRESS framework (Kim et al. 2020a,c, and this work) than the idealized simulations with a fixed p_* (Shetty & Ostriker 2012; Kim et al. 2013; Kim & Ostriker 2015a).

In the present simulations, an additional effect comes into play to reduce p_* : many SNe explode slightly exterior to the ring or close to the ring boundary, dumping their energy into the ambient hot gas and bulk motions of the ring instead of driving internal turbulence within the ring. This could be the primary reason for the smaller turbulent yield in our simulations compared to TIGRESS simulations where the momentum is more fully captured by the surrounding warm-cold gas. Additionally, when SNe are very crowded, partial cancellation of the vertical momenta due to interactions of neighboring shells could also contribute to reducing Υ_{turb} . All of these considerations explain why SN feedback is somewhat less efficient in driving turbulence within star-forming nuclear ring regions compared to outer disk environments.

Depletion time—The depletion time measured in our simulations, $t_{\text{dep,ring}} \sim 10 - 100$ Myr, is very short compared to the solar neighborhood TIGRESS model (~ 2 Gyr; Kim & Ostriker 2017), although analogous TIGRESS simulations modeling regions with higher gas and stellar density – closer to those of the present models – have $t_{\text{dep}} \sim 70 - 400$ Myr (Kim et al. 2020a). If star formation is locally regulated by stellar feedback (including SNe), the depletion time is determined by

balancing the ISM weight $\mathcal{W} = (\Sigma/2) \langle g_z \rangle$ and the mid-plane pressure $P_{\text{mid}} \equiv \Upsilon_{\text{tot}} \Sigma_{\text{SFR}} \equiv \Upsilon_{\text{tot}} \Sigma / t_{\text{dep}}$, such that $t_{\text{dep}} = 2\Upsilon_{\text{tot}} / \langle g_z \rangle$. Here, Σ is the local gas surface density (equivalent to Σ_{ring} for the present case), $\langle g_z \rangle$ denotes the mass-weighted vertical gravity, and Υ_{tot} is the total feedback yield. The analysis given in Section 4.2 suggests that the short t_{dep} of the present simulations results from the combined effect of reduced Υ_{tot} (see above) and strong $\langle g_z \rangle$, with the latter being more important. Similar to our results, Sormani et al. (2020) found from analysis of their simulations that the decrease in the CMZ $t_{\text{dep}} \sim 100$ Myr compared to the outer region $t_{\text{dep}} \sim (1 - 2)$ Gyr was consistent with expectations from self-regulation, with $\langle g_z \rangle$ dominated by the stellar potential. The small depletion time in our galactic center simulations together with the result that the gravitational field is dominated by the stellar component (including newly-formed stars) appears qualitatively consistent with Utomo et al. (2017). They found that $\sim 30\%$ of the EDGE galaxy sample have a central drop in t_{dep} , and that the drop in t_{dep} is correlated with a central increase in stellar surface density.

Our depletion time is still much shorter than observational values of $10^2 - 10^3$ Myr for most galactic centers and starburst galaxies, although observed values can be as short as 3 - 10 Myr in regions of extremely high surface density (Kennicutt 1998; Bigiel et al. 2008; Genzel et al. 2010; Narayanan et al. 2012; Utomo et al. 2017; Wilson et al. 2019). Also, observations using the DYNAMO sample – local analogues of clumpy, high redshift ($z \sim 1 - 2$) galaxies – have suggested there may be superlinear pressure enhancement in regions with high Σ_{SFR} (Fisher et al. 2019), although these regions are not well resolved spatially, and the trend is moderated when molecular gas (instead of ionized gas) velocity dispersions are used to estimate the ISM weight (Girard et al. 2021). Molina et al. (2020) find an upper limit on pressure slightly above the prediction of Equation (33). While higher-resolution observations are essential (and improved estimates of the stellar gravity are needed), current empirical work indicates that our models for star formation and feedback cannot fully explain real galaxies at high SFRs.

Several physical elements not yet included in the present models may explain the lower t_{dep} than in real galaxies. First, our current models only include FUV and CR heating and Type II SNe, while neglecting magnetic fields, CR pressure, and forms of early feedback (see below). All of these contribute to support and/or dispersal of the large-scale ISM and/or individual clouds, and thus may help to lengthen the depletion time (e.g., Hennebelle & Iffrig 2014; Kim & Ostriker

2015a; Girichidis et al. 2016; Kim et al. 2020a,b,c). For instance, typical magnetic fields in nuclear rings are of order $\sim 60 \mu\text{G}$ (see Beck 2015, and references therein). The corresponding magnetic pressure is $P_{\text{mag}}/k_B \sim 1 \times 10^6 \text{ K cm}^{-3}$, which can be dynamically significant.

Second, since we do not model the destruction of star clusters, the old, massive sink particles remain concentrated at the midplane, increasing \mathcal{W}_{sp} and $\langle g_z \rangle$ and thus reducing t_{dep} . In reality, however, they are expected to be disrupted and dispersed both radially and vertically by cluster-cluster collisions and/or the tidal gravity (e.g., Portegies Zwart et al. 2002; de Grijs & Anders 2012; Väisänen et al. 2014), reducing Σ_{sp} and increasing t_{dep} .

Third, in this paper we do not model early feedback such as stellar winds, photoionization, and radiation pressure from young stars, which can disperse natal clouds even before the onset of the first SNe, limiting their lifetime star formation efficiency (e.g., Rogers & Pittard 2013; Rahner et al. 2017; Kim et al. 2018b, 2020b). Rather than our simple model of 100% star formation efficiency when sink particles form, a more realistic treatment would include significant mass return over several Myr. Since the total momentum injection from early feedback is low compared to the injection from SNe (Kim et al. 2018b, L. Lancaster et al 2021, submitted), these processes are not likely to alter large-scale SFRs in outer-galaxy environments where dynamical times within clouds are several Myr. However, early feedback is potentially quite important in denser galactic-center environments.

Finally, we remark that inclusion of these physical elements may lead to stronger and/or more localized star

formation and ensuing feedback. In this case, the rings may become more prone to local destruction, and the SFR and the depletion time may exhibit large temporal fluctuations, even if the mass inflow rate is kept constant. Assessing the relation between the ring SFR and the mass inflow rate would thus require more realistic treatments of star formation and feedback.

ACKNOWLEDGEMENTS

We acknowledge an insightful and constructive report from the referee. We thank Jeong-Gyu Kim for useful discussions and help in radiation post-processing for the development of the approximate form of FUV heating rate. We thank Munan Gong for highlighting the importance of CR heating and suggesting an approximate form for the CR heating rate. The work of S.M. was supported by an NRF (National Research Foundation of Korea) grant funded by the Korean Government (NRF-2017H1A2A1043558-Fostering Core Leaders of the Future Basic Science Program/Global Ph.D. Fellowship Program). The work of W.-T.K. was supported by the grants of National Research Foundation of Korea (2019R1A2C1004857 and 2020R1A4A2002885). The work of E.C.O and C.-G.K. was partly supported by NASA (ATP grant No. NNX17AG26G). Computational resources for this project were provided by Princeton Research Computing, a consortium including PICSciE and OIT at Princeton University, and by the Supercomputing Center/Korea Institute of Science and Technology Information with supercomputing resources including technical support (KSC-2019-CRE-0052).

Software: Athena (Stone et al. 2008), STARBURST99 (Leitherer et al. 1999)

APPENDIX

A. ORBIT INTEGRATION OF SINK PARTICLES WITH THE CORIOLIS FORCE

Here we describe how we apply the Boris algorithm, which is widely used in plasma simulations, to integrate the equations of motion for sink particles in a rotating frame; we also present a test result. Note that Equation (14) is formally equivalent to the equations of motion for charged particles under the Lorentz force if we substitute $-\nabla\Phi_{\text{tot}} \rightarrow q\mathbf{E}/m$ and $2\mathbf{\Omega}_p \rightarrow q\mathbf{B}/m$.

As in the original TIGRESS implementation, we adopt a ‘‘Kick-Drift-Kick (KDK)’’ leap-frog integrator, for which a semi-implicit discretization of Equation (14) leads to

$$\frac{\mathbf{v}^{n+1/2} - \mathbf{v}^{n-1/2}}{\Delta t} = \mathbf{g}^n - 2\mathbf{\Omega}_p \times \left(\frac{\mathbf{v}^{n+1/2} + \mathbf{v}^{n-1/2}}{2} \right), \quad (\text{A1})$$

where $\mathbf{g} = -\nabla\Phi_{\text{tot}}$ is the gravitational acceleration. Boris (1970) noted that the “electric” and “magnetic” forces in Equation (A1) can be separated by changing the variables to

$$\mathbf{v}^- \equiv \mathbf{v}^{n-1/2} + \frac{\Delta t}{2} \mathbf{g}^n, \quad (\text{A2})$$

$$\mathbf{v}^+ \equiv \mathbf{v}^{n+1/2} - \frac{\Delta t}{2} \mathbf{g}^n, \quad (\text{A3})$$

yielding

$$\frac{\mathbf{v}^+ - \mathbf{v}^-}{\Delta t} = (\mathbf{v}^+ + \mathbf{v}^-) \times \boldsymbol{\Omega}_p. \quad (\text{A4})$$

Taking the inner product of Equation (A4) with $(\mathbf{v}^+ + \mathbf{v}^-)$ reveals $|\mathbf{v}^+| = |\mathbf{v}^-|$, i.e., Equation (A4) describes a pure rotation of the vector \mathbf{v}^- into \mathbf{v}^+ , with $\boldsymbol{\Omega}_p$ being the axis of the rotation, as depicted in Figure 21. It can be shown that the rotation angle θ in Figure 21 satisfies $\tan(\theta/2) = \Omega_p \Delta t$. Assuming $\boldsymbol{\Omega}_p$ is parallel to the z -axis, Equation (A4) can be decomposed to

$$v_x^+ = \frac{1 - (\Omega_p \Delta t)^2}{1 + (\Omega_p \Delta t)^2} v_x^- + \frac{2\Omega_p \Delta t}{1 + (\Omega_p \Delta t)^2} v_y^-, \quad (\text{A5})$$

$$v_y^+ = -\frac{2\Omega_p \Delta t}{1 + (\Omega_p \Delta t)^2} v_x^- + \frac{1 - (\Omega_p \Delta t)^2}{1 + (\Omega_p \Delta t)^2} v_y^-, \quad (\text{A6})$$

$$v_z^+ = v_z^-. \quad (\text{A7})$$

In the Boris algorithm, therefore, it takes three steps to update $\mathbf{v}^{n-1/2}$ to $\mathbf{v}^{n+1/2}$. (1) Apply the gravitational force for a half time step as in Equation (A2), (2) solve for the epicyclic rotation using Equation (A5)–(A7), and (3) apply the gravitational force for the remaining half time step according to Equation (A3).

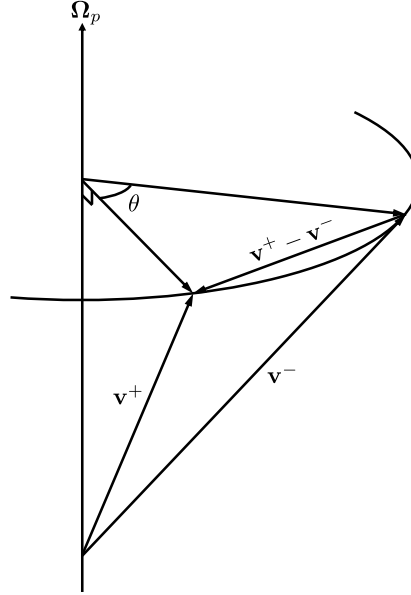


Figure 21. Illustration of the velocity vector rotation described by Equation (A4). The rotation angle θ is defined in the plane perpendicular to $\boldsymbol{\Omega}_p$.

As a test calculation, we consider a particle orbiting solely under a rotating, rigid-body potential $\Phi_{\text{ext}} = \frac{1}{2}R^2\Omega_0^2$ with $\Omega_0 = 1$, $\Omega_p = 0.5$ and $\Phi_{\text{self}} = 0$. The orbit is limited to the $z = 0$ plane. The equations of motion for such a particle are given by

$$\ddot{x} = -(\Omega_0^2 - \Omega_p^2)x + 2\Omega_p \dot{y}, \quad (\text{A8a})$$

$$\ddot{y} = -(\Omega_0^2 - \Omega_p^2)y - 2\Omega_p \dot{x}. \quad (\text{A8b})$$

Equations (A8a)–(A8b) are linear, coupled ordinary differential equations with analytic solutions

$$x(t) = A_1 \cos(\Omega_- t) + A_2 \sin(\Omega_- t) + A_3 \cos(\Omega_+ t) + A_4 \sin(\Omega_+ t), \quad (\text{A9a})$$

$$y(t) = -A_2 \cos(\Omega_- t) + A_1 \sin(\Omega_- t) + A_4 \cos(\Omega_+ t) - A_3 \sin(\Omega_+ t), \quad (\text{A9b})$$

where $\Omega_{\pm} \equiv \Omega_0 \pm \Omega_p$ and

$$A_1 = (\Omega_+ x(0) + \dot{y}(0))/(2\Omega_0), \quad (\text{A10})$$

$$A_2 = (\dot{x}(0) - \Omega_+ y(0))/(2\Omega_0), \quad (\text{A11})$$

$$A_3 = (\Omega_- x(0) - \dot{y}(0))/(2\Omega_0), \quad (\text{A12})$$

$$A_4 = (\dot{x}(0) + \Omega_- y(0))/(2\Omega_0), \quad (\text{A13})$$

with initial position $[x(0), y(0)]$ and velocity $[\dot{x}(0), \dot{y}(0)]$.

As the initial conditions, we take $(x, y) = (1, 0)$ and $(\dot{x}, \dot{y}) = (0, 2)$ at $t = 0$ and integrate Equation (A8) using the Boris algorithm with a fixed timestep of $\Delta t = 0.1/\Omega_0$. For comparison, we also integrate Equation (A8) using the standard KDK leap-frog integrator. Figure 22 compares the resulting orbits in the x - y plane, the position offsets relative to the analytic predictions (Equation A9), and the errors in the Jacobi integral $E_J \equiv \frac{1}{2}(\dot{x}^2 + \dot{y}^2) + \Phi_{\text{tot}}$. The position offsets oscillate and secularly grow with time in both methods, but the growth rate is much lower in the Boris algorithm. The relative errors in the Jacobi integral are bounded below 0.2% in the Boris algorithm.

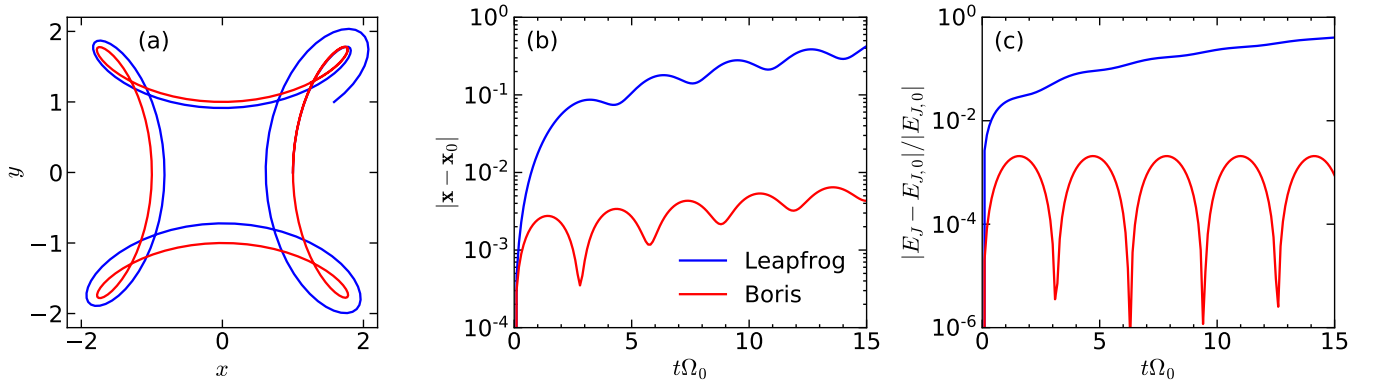


Figure 22. Comparison between the Boris algorithm (red) and the standard leap-frog integrator (blue) for (a) the particle orbits in the x - y plane, (b) the position offsets between the numerical and analytic solutions, and (c) the relative errors in the Jacobi integral E_J under the rotating, rigid-body potential $\Phi_{\text{ext}} = \frac{1}{2}R^2\Omega_0^2$ with $\Omega_0 = 1$ and $\Omega_p = 0.5$. The initial conditions are $(x, y) = (1, 0)$ and $(\dot{x}, \dot{y}) = (0, 2)$ and $\Delta t = 0.1/\Omega_0$ is taken for the timestep.

REFERENCES

- Allard, E. L., Knapen, J. H., Peletier, R. F., & Sarzi, M. 2006, *MNRAS*, 371, 1087, doi: [10.1111/j.1365-2966.2006.10751.x](https://doi.org/10.1111/j.1365-2966.2006.10751.x)
- Armillotta, L., Krumholz, M. R., Di Teodoro, E. M., & McClure-Griffiths, N. M. 2019, *MNRAS*, 2479, doi: [10.1093/mnras/stz2880](https://doi.org/10.1093/mnras/stz2880)
- Athanassoula, E. 1992, *MNRAS*, 259, 345, doi: [10.1093/mnras/259.2.345](https://doi.org/10.1093/mnras/259.2.345)
- Athanassoula, E. 1994, in *Mass-Transfer Induced Activity in Galaxies*, ed. I. Shlosman, 143
- Barnes, A. T., Longmore, S. N., Battersby, C., et al. 2017, *MNRAS*, 469, 2263, doi: [10.1093/mnras/stx941](https://doi.org/10.1093/mnras/stx941)
- Beck, R. 2015, *A&A Rv*, 24, 4, doi: [10.1007/s00159-015-0084-4](https://doi.org/10.1007/s00159-015-0084-4)
- Bigiel, F., Leroy, A., Walter, F., et al. 2008, *AJ*, 136, 2846, doi: [10.1088/0004-6256/136/6/2846](https://doi.org/10.1088/0004-6256/136/6/2846)
- Binney, J., Gerhard, O. E., Stark, A. A., Bally, J., & Uchida, K. I. 1991, *MNRAS*, 252, 210, doi: [10.1093/mnras/252.2.210](https://doi.org/10.1093/mnras/252.2.210)
- Boris, J. P. 1970, in *Proc. Fourth Conf. Num. Sim. Plasmas*, 3–67

- Boulares, A., & Cox, D. P. 1990, *ApJ*, 365, 544, doi: [10.1086/169509](https://doi.org/10.1086/169509)
- Buta, R. 1986, *ApJS*, 61, 609, doi: [10.1086/191126](https://doi.org/10.1086/191126)
- Buta, R., & Combes, F. 1996, *FCPh*, 17, 95
- Combes, F. 2001, in *Advanced Lectures on the Starburst-AGN*, ed. I. Aretxaga, D. Kunth, & R. Mújica, 223, doi: [10.1142/9789812811318_0006](https://doi.org/10.1142/9789812811318_0006)
- Combes, F., & Gerin, M. 1985, *A&A*, 150, 327
- Comerón, S., Knapen, J. H., Beckman, J. E., et al. 2010, *MNRAS*, 402, 2462, doi: [10.1111/j.1365-2966.2009.16057.x](https://doi.org/10.1111/j.1365-2966.2009.16057.x)
- Comerón, S., Martínez-Valpuesta, I., Knapen, J. H., & Beckman, J. E. 2009, *ApJL*, 706, L256, doi: [10.1088/0004-637X/706/2/L256](https://doi.org/10.1088/0004-637X/706/2/L256)
- de Grijs, R., & Anders, P. 2012, *ApJL*, 758, L22, doi: [10.1088/2041-8205/758/1/L22](https://doi.org/10.1088/2041-8205/758/1/L22)
- Draine, B. T. 1978, *ApJS*, 36, 595, doi: [10.1086/190513](https://doi.org/10.1086/190513)
- . 2011, *Physics of the Interstellar and Intergalactic Medium* (Princeton University Press)
- Elmegreen, B. G. 1994, *ApJL*, 425, L73, doi: [10.1086/187313](https://doi.org/10.1086/187313)
- Elmegreen, B. G., & Parravano, A. 1994, *ApJL*, 435, L121, doi: [10.1086/187609](https://doi.org/10.1086/187609)
- Englmaier, P., & Gerhard, O. 1997, *MNRAS*, 287, 57, doi: [10.1093/mnras/287.1.57](https://doi.org/10.1093/mnras/287.1.57)
- Fielding, D., Quataert, E., Martizzi, D., & Faucher-Giguère, C.-A. 2017, *MNRAS*, 470, L39, doi: [10.1093/mnrasl/slx072](https://doi.org/10.1093/mnrasl/slx072)
- Fisher, D. B., Bolatto, A. D., White, H., et al. 2019, *ApJ*, 870, 46, doi: [10.3847/1538-4357/aaee8b](https://doi.org/10.3847/1538-4357/aaee8b)
- Gadotti, D. A., Sánchez-Blázquez, P., Falcón-Barroso, J., et al. 2019, *MNRAS*, 482, 506, doi: [10.1093/mnras/sty2666](https://doi.org/10.1093/mnras/sty2666)
- García-Barreto, J. A., Downes, D., Combes, F., et al. 1991, *A&A*, 244, 257
- Genzel, R., Tacconi, L. J., Gracia-Carpio, J., et al. 2010, *MNRAS*, 407, 2091, doi: [10.1111/j.1365-2966.2010.16969.x](https://doi.org/10.1111/j.1365-2966.2010.16969.x)
- Ginsburg, A., Henkel, C., Ao, Y., et al. 2016, *A&A*, 586, A50, doi: [10.1051/0004-6361/201526100](https://doi.org/10.1051/0004-6361/201526100)
- Girard, M., Fisher, D. B., Bolatto, A. D., et al. 2021, *arXiv e-prints*, arXiv:2101.04122, <https://arxiv.org/abs/2101.04122>
- Girichidis, P., Naab, T., Walch, S., et al. 2016, *ApJL*, 816, L19, doi: [10.3847/2041-8205/816/2/L19](https://doi.org/10.3847/2041-8205/816/2/L19)
- Gong, M., Ostriker, E. C., & Wolfire, M. G. 2017, *ApJ*, 843, 38, doi: [10.3847/1538-4357/aa7561](https://doi.org/10.3847/1538-4357/aa7561)
- Harada, N., Sakamoto, K., Martín, S., et al. 2019, *ApJ*, 884, 100, doi: [10.3847/1538-4357/ab41ff](https://doi.org/10.3847/1538-4357/ab41ff)
- Harris, J., Calzetti, D., Gallagher, John S., I., Conselice, C. J., & Smith, D. A. 2001, *AJ*, 122, 3046, doi: [10.1086/324230](https://doi.org/10.1086/324230)
- Hennabelle, P., & Iffrig, O. 2014, *A&A*, 570, A81, doi: [10.1051/0004-6361/201423392](https://doi.org/10.1051/0004-6361/201423392)
- Henshaw, J. D., Longmore, S. N., Kruijssen, J. M. D., et al. 2016, *MNRAS*, 457, 2675, doi: [10.1093/mnras/stw121](https://doi.org/10.1093/mnras/stw121)
- Hopkins, P. F. 2015, *MNRAS*, 450, 53, doi: [10.1093/mnras/stv195](https://doi.org/10.1093/mnras/stv195)
- Hsieh, P.-Y., Matsushita, S., Liu, G., et al. 2011, *ApJ*, 736, 129, doi: [10.1088/0004-637X/736/2/129](https://doi.org/10.1088/0004-637X/736/2/129)
- Immer, K., Schuller, F., Omont, A., & Menten, K. M. 2012, *A&A*, 537, A121, doi: [10.1051/0004-6361/201117857](https://doi.org/10.1051/0004-6361/201117857)
- Kennicutt, Robert C., J. 1994, in *Mass-Transfer Induced Activity in Galaxies*, ed. I. Shlosman, 131
- Kennicutt, Robert C., J. 1998, *ApJ*, 498, 541, doi: [10.1086/305588](https://doi.org/10.1086/305588)
- Kennicutt, R. C., & Evans, N. J. 2012, *ARA&A*, 50, 531, doi: [10.1146/annurev-astro-081811-125610](https://doi.org/10.1146/annurev-astro-081811-125610)
- Kim, C.-G., Kim, W.-T., & Ostriker, E. C. 2008, *ApJ*, 681, 1148, doi: [10.1086/588752](https://doi.org/10.1086/588752)
- . 2011a, *ApJ*, 743, 25, doi: [10.1088/0004-637X/743/1/25](https://doi.org/10.1088/0004-637X/743/1/25)
- Kim, C.-G., & Ostriker, E. C. 2015a, *ApJ*, 815, 67, doi: [10.1088/0004-637X/815/1/67](https://doi.org/10.1088/0004-637X/815/1/67)
- . 2015b, *ApJ*, 802, 99, doi: [10.1088/0004-637X/802/2/99](https://doi.org/10.1088/0004-637X/802/2/99)
- . 2017, *ApJ*, 846, 133, doi: [10.3847/1538-4357/aa8599](https://doi.org/10.3847/1538-4357/aa8599)
- . 2018, *ApJ*, 853, 173, doi: [10.3847/1538-4357/aaa5ff](https://doi.org/10.3847/1538-4357/aaa5ff)
- Kim, C.-G., Ostriker, E. C., & Kim, W.-T. 2013, *ApJ*, 776, 1, doi: [10.1088/0004-637X/776/1/1](https://doi.org/10.1088/0004-637X/776/1/1)
- Kim, C.-G., Ostriker, E. C., & Raileanu, R. 2017a, *ApJ*, 834, 25, doi: [10.3847/1538-4357/834/1/25](https://doi.org/10.3847/1538-4357/834/1/25)
- Kim, C.-G., Ostriker, E. C., Somerville, R. S., et al. 2020a, *ApJ*, 900, 61, doi: [10.3847/1538-4357/aba962](https://doi.org/10.3847/1538-4357/aba962)
- Kim, E., Kim, S. S., Choi, Y.-Y., et al. 2018a, *MNRAS*, 479, 562, doi: [10.1093/mnras/sty1451](https://doi.org/10.1093/mnras/sty1451)
- Kim, J.-G., Kim, W.-T., & Ostriker, E. C. 2018b, *ApJ*, 859, 68, doi: [10.3847/1538-4357/aabe27](https://doi.org/10.3847/1538-4357/aabe27)
- Kim, J.-G., Kim, W.-T., Ostriker, E. C., & Skinner, M. A. 2017b, *ApJ*, 851, 93, doi: [10.3847/1538-4357/aa9b80](https://doi.org/10.3847/1538-4357/aa9b80)
- Kim, J.-G., Ostriker, E. C., & Filippova, N. 2020b, *arXiv e-prints*, arXiv:2011.07772, <https://arxiv.org/abs/2011.07772>
- Kim, S. S., Saitoh, T. R., Jeon, M., et al. 2011b, *ApJL*, 735, L11, doi: [10.1088/2041-8205/735/1/L11](https://doi.org/10.1088/2041-8205/735/1/L11)
- Kim, W.-T., Kim, C.-G., & Ostriker, E. C. 2020c, *ApJ*, 898, 35, doi: [10.3847/1538-4357/ab9b87](https://doi.org/10.3847/1538-4357/ab9b87)
- Kim, W.-T., Seo, W.-Y., & Kim, Y. 2012a, *ApJ*, 758, 14, doi: [10.1088/0004-637X/758/1/14](https://doi.org/10.1088/0004-637X/758/1/14)

- Kim, W.-T., Seo, W.-Y., Stone, J. M., Yoon, D., & Teuben, P. J. 2012b, *ApJ*, 747, 60, doi: [10.1088/0004-637X/747/1/60](https://doi.org/10.1088/0004-637X/747/1/60)
- Kim, W.-T., & Stone, J. M. 2012, *ApJ*, 751, 124, doi: [10.1088/0004-637X/751/2/124](https://doi.org/10.1088/0004-637X/751/2/124)
- Kim, Y., & Kim, W.-T. 2014, *MNRAS*, 440, 208, doi: [10.1093/mnras/stu276](https://doi.org/10.1093/mnras/stu276)
- Koepferl, C. M., Robitaille, T. P., Morales, E. F. E., & Johnston, K. G. 2015, *ApJ*, 799, 53, doi: [10.1088/0004-637X/799/1/53](https://doi.org/10.1088/0004-637X/799/1/53)
- Kormendy, J., & Kennicutt, Robert C., J. 2004, *ARA&A*, 42, 603, doi: [10.1146/annurev.astro.42.053102.134024](https://doi.org/10.1146/annurev.astro.42.053102.134024)
- Koyama, H., & Inutsuka, S.-i. 2002, *ApJL*, 564, L97, doi: [10.1086/338978](https://doi.org/10.1086/338978)
- Kroupa, P. 2001, *MNRAS*, 322, 231, doi: [10.1046/j.1365-8711.2001.04022.x](https://doi.org/10.1046/j.1365-8711.2001.04022.x)
- Kruijssen, J. M. D., Longmore, S. N., Elmegreen, B. G., et al. 2014, *MNRAS*, 440, 3370, doi: [10.1093/mnras/stu494](https://doi.org/10.1093/mnras/stu494)
- Krumholz, M. R., & Kruijssen, J. M. D. 2015, *MNRAS*, 453, 739, doi: [10.1093/mnras/stv1670](https://doi.org/10.1093/mnras/stv1670)
- Krumholz, M. R., Kruijssen, J. M. D., & Crocker, R. M. 2017, *MNRAS*, 466, 1213, doi: [10.1093/mnras/stw3195](https://doi.org/10.1093/mnras/stw3195)
- Leitherer, C., Schaerer, D., Goldader, J. D., et al. 1999, *ApJS*, 123, 3, doi: [10.1086/313233](https://doi.org/10.1086/313233)
- Lemaster, M. N., & Stone, J. M. 2009, *ApJ*, 691, 1092, doi: [10.1088/0004-637X/691/2/1092](https://doi.org/10.1088/0004-637X/691/2/1092)
- Li, Z., Shen, J., & Kim, W.-T. 2015, *ApJ*, 806, 150, doi: [10.1088/0004-637X/806/2/150](https://doi.org/10.1088/0004-637X/806/2/150)
- Longmore, S. N., Bally, J., Testi, L., et al. 2013, *MNRAS*, 429, 987, doi: [10.1093/mnras/sts376](https://doi.org/10.1093/mnras/sts376)
- Ma, C., de Grijs, R., & Ho, L. C. 2018, *ApJ*, 857, 116, doi: [10.3847/1538-4357/aab6b4](https://doi.org/10.3847/1538-4357/aab6b4)
- Martizzi, D., Faucher-Giguère, C.-A., & Quataert, E. 2015, *MNRAS*, 450, 504, doi: [10.1093/mnras/stv562](https://doi.org/10.1093/mnras/stv562)
- Martizzi, D., Fielding, D., Faucher-Giguère, C.-A., & Quataert, E. 2016, *MNRAS*, 459, 2311, doi: [10.1093/mnras/stw745](https://doi.org/10.1093/mnras/stw745)
- Mazzuca, L. M., Knapen, J. H., Veilleux, S., & Regan, M. W. 2008, *ApJS*, 174, 337, doi: [10.1086/522338](https://doi.org/10.1086/522338)
- Molina, J., Ibar, E., Godoy, N., et al. 2020, *A&A*, 643, A78, doi: [10.1051/0004-6361/202039008](https://doi.org/10.1051/0004-6361/202039008)
- Molinari, S., Bally, J., Noriega-Crespo, A., et al. 2011, *ApJ*, 735, L33, doi: [10.1088/2041-8205/735/2/L33](https://doi.org/10.1088/2041-8205/735/2/L33)
- Morgan, W. W. 1958, *PASP*, 70, 364, doi: [10.1086/127243](https://doi.org/10.1086/127243)
- Narayanan, D., Krumholz, M. R., Ostriker, E. C., & Hernquist, L. 2012, *MNRAS*, 421, 3127, doi: [10.1111/j.1365-2966.2012.20536.x](https://doi.org/10.1111/j.1365-2966.2012.20536.x)
- Neufeld, D. A., & Wolfire, M. G. 2017, *ApJ*, 845, 163, doi: [10.3847/1538-4357/aa6d68](https://doi.org/10.3847/1538-4357/aa6d68)
- Onishi, K., Iguchi, S., Sheth, K., & Kohno, K. 2015, *ApJ*, 806, 39, doi: [10.1088/0004-637X/806/1/39](https://doi.org/10.1088/0004-637X/806/1/39)
- Orr, M. E., Hayward, C. C., Medling, A. M., et al. 2020, *MNRAS*, 496, 1620, doi: [10.1093/mnras/staa1619](https://doi.org/10.1093/mnras/staa1619)
- Ostriker, E. C., McKee, C. F., & Leroy, A. K. 2010, *ApJ*, 721, 975, doi: [10.1088/0004-637X/721/2/975](https://doi.org/10.1088/0004-637X/721/2/975)
- Ostriker, E. C., & Shetty, R. 2011, *ApJ*, 731, 41, doi: [10.1088/0004-637X/731/1/41](https://doi.org/10.1088/0004-637X/731/1/41)
- Patsis, P. A., & Athanassoula, E. 2000, *A&A*, 358, 45
- Piñol-Ferrer, N., Fathi, K., Carignan, C., et al. 2014, *MNRAS*, 438, 971, doi: [10.1093/mnras/stt2162](https://doi.org/10.1093/mnras/stt2162)
- Pierce-Price, D., Richer, J. S., Greaves, J. S., et al. 2000, *ApJ*, 545, L121, doi: [10.1086/317884](https://doi.org/10.1086/317884)
- Piner, B. G., Stone, J. M., & Teuben, P. J. 1995, *ApJ*, 449, 508, doi: [10.1086/176075](https://doi.org/10.1086/176075)
- Portegies Zwart, S. F., Makino, J., McMillan, S. L. W., & Hut, P. 2002, *ApJ*, 565, 265, doi: [10.1086/324141](https://doi.org/10.1086/324141)
- Rahner, D., Pellegrini, E. W., Glover, S. C. O., & Klessen, R. S. 2017, *MNRAS*, 470, 4453, doi: [10.1093/mnras/stx1532](https://doi.org/10.1093/mnras/stx1532)
- Regan, M. W., & Teuben, P. 2003, *ApJ*, 582, 723, doi: [10.1086/344721](https://doi.org/10.1086/344721)
- Rogers, H., & Pittard, J. M. 2013, *MNRAS*, 431, 1337, doi: [10.1093/mnras/stt255](https://doi.org/10.1093/mnras/stt255)
- Sanders, R., Morano, E., & Druguet, M.-C. 1998, *Journal of Computational Physics*, 145, 511, doi: [10.1006/jcph.1998.6047](https://doi.org/10.1006/jcph.1998.6047)
- Sarzi, M., Allard, E. L., Knapen, J. H., & Mazzuca, L. M. 2007, *MNRAS*, 380, 949, doi: [10.1111/j.1365-2966.2007.12177.x](https://doi.org/10.1111/j.1365-2966.2007.12177.x)
- Schmidt, M. 1959, *ApJ*, 129, 243, doi: [10.1086/146614](https://doi.org/10.1086/146614)
- Schneider, E. E., Robertson, B. E., & Thompson, T. A. 2018, *ApJ*, 862, 56, doi: [10.3847/1538-4357/aacce1](https://doi.org/10.3847/1538-4357/aacce1)
- Seo, W.-Y., & Kim, W.-T. 2013, *ApJ*, 769, 100, doi: [10.1088/0004-637X/769/2/100](https://doi.org/10.1088/0004-637X/769/2/100)
- . 2014, *ApJ*, 792, 47, doi: [10.1088/0004-637X/792/1/47](https://doi.org/10.1088/0004-637X/792/1/47)
- Seo, W.-Y., Kim, W.-T., Kwak, S., et al. 2019, *ApJ*, 872, 5, doi: [10.3847/1538-4357/aafc5f](https://doi.org/10.3847/1538-4357/aafc5f)
- Sérsic, J. L., & Pastoriza, M. 1965, *PASP*, 77, 287, doi: [10.1086/128217](https://doi.org/10.1086/128217)
- Sheth, K., Vogel, S. N., Regan, M. W., Thornley, M. D., & Teuben, P. J. 2005, *ApJ*, 632, 217, doi: [10.1086/432409](https://doi.org/10.1086/432409)
- Shetty, R., & Ostriker, E. C. 2012, *ApJ*, 754, 2, doi: [10.1088/0004-637X/754/1/2](https://doi.org/10.1088/0004-637X/754/1/2)
- Shin, J., Kim, S. S., Baba, J., et al. 2017, *ApJ*, 841, 74, doi: [10.3847/1538-4357/aa7061](https://doi.org/10.3847/1538-4357/aa7061)
- Shlosman, I., Begelman, M. C., & Frank, J. 1990, *Nature*, 345, 679, doi: [10.1038/345679a0](https://doi.org/10.1038/345679a0)
- Skinner, M. A., & Ostriker, E. C. 2015, *ApJ*, 809, 187, doi: [10.1088/0004-637X/809/2/187](https://doi.org/10.1088/0004-637X/809/2/187)

- Sormani, M. C., & Barnes, A. T. 2019, MNRAS, 484, 1213, doi: [10.1093/mnras/stz046](https://doi.org/10.1093/mnras/stz046)
- Sormani, M. C., Binney, J., & Magorrian, J. 2015, MNRAS, 449, 2421, doi: [10.1093/mnras/stv441](https://doi.org/10.1093/mnras/stv441)
- Sormani, M. C., Sobacchi, E., Fragkoudi, F., et al. 2018, MNRAS, 481, 2, doi: [10.1093/mnras/sty2246](https://doi.org/10.1093/mnras/sty2246)
- Sormani, M. C., Tress, R. G., Glover, S. C. O., et al. 2020, arXiv e-prints, arXiv:2004.06731. <https://arxiv.org/abs/2004.06731>
- Springel, V. 2010, MNRAS, 401, 791, doi: [10.1111/j.1365-2966.2009.15715.x](https://doi.org/10.1111/j.1365-2966.2009.15715.x)
- Sternberg, A., McKee, C. F., & Wolfire, M. G. 2002, ApJS, 143, 419, doi: [10.1086/343032](https://doi.org/10.1086/343032)
- Stone, J. M., & Gardiner, T. 2009, NewA, 14, 139, doi: [10.1016/j.newast.2008.06.003](https://doi.org/10.1016/j.newast.2008.06.003)
- Stone, J. M., Gardiner, T. A., Teuben, P., Hawley, J. F., & Simon, J. B. 2008, ApJS, 178, 137, doi: [10.1086/588755](https://doi.org/10.1086/588755)
- Strickland, D. K., Heckman, T. M., Colbert, E. J. M., Hoopes, C. G., & Weaver, K. A. 2004, ApJS, 151, 193, doi: [10.1086/382214](https://doi.org/10.1086/382214)
- Sutherland, R. S., & Dopita, M. A. 1993, ApJS, 88, 253, doi: [10.1086/191823](https://doi.org/10.1086/191823)
- Tokuyama, S., Oka, T., Takekawa, S., et al. 2019, PASJ, doi: [10.1093/pasj/psy150](https://doi.org/10.1093/pasj/psy150)
- Torrey, P., Hopkins, P. F., Faucher-Giguère, C.-A., et al. 2017, MNRAS, 467, 2301, doi: [10.1093/mnras/stx254](https://doi.org/10.1093/mnras/stx254)
- Tress, R. G., Sormani, M. C., Glover, S. C. O., et al. 2020, arXiv e-prints, arXiv:2004.06724. <https://arxiv.org/abs/2004.06724>
- Utomo, D., Bolatto, A. D., Wong, T., et al. 2017, ApJ, 849, 26, doi: [10.3847/1538-4357/aa88c0](https://doi.org/10.3847/1538-4357/aa88c0)
- Väisänen, P., Barway, S., & Rämmin, A. 2014, ApJL, 797, L16, doi: [10.1088/2041-8205/797/2/L16](https://doi.org/10.1088/2041-8205/797/2/L16)
- Wada, K., Papadopoulos, P. P., & Spaans, M. 2009, ApJ, 702, 63, doi: [10.1088/0004-637X/702/1/63](https://doi.org/10.1088/0004-637X/702/1/63)
- Weinberger, R., Springel, V., & Pakmor, R. 2020, ApJS, 248, 32, doi: [10.3847/1538-4365/ab908c](https://doi.org/10.3847/1538-4365/ab908c)
- Wilson, C. D., Elmegreen, B. G., Bemis, A., & Brunetti, N. 2019, ApJ, 882, 5, doi: [10.3847/1538-4357/ab31f3](https://doi.org/10.3847/1538-4357/ab31f3)
- Wolfire, M. G., McKee, C. F., Hollenbach, D., & Tielens, A. G. G. M. 2003, ApJ, 587, 278, doi: [10.1086/368016](https://doi.org/10.1086/368016)
- Yukita, M., Swartz, D. A., Tennant, A. F., Soria, R., & Irwin, J. A. 2012, ApJ, 758, 105, doi: [10.1088/0004-637X/758/2/105](https://doi.org/10.1088/0004-637X/758/2/105)
- Yusef-Zadeh, F., Hewitt, J. W., Arendt, R. G., et al. 2009, ApJ, 702, 178, doi: [10.1088/0004-637X/702/1/178](https://doi.org/10.1088/0004-637X/702/1/178)